universität wien

MASTERARBEIT | MASTER'S THESIS

Titel | Title

Computational Study of Different Bond Cleavage Selectivity in Triflate-Based Organic Compounds

verfasst von | submitted by

Constantin Richard Feitl BSc

angestrebter akademischer Grad | in partial fulfilment of the requirements for the degree of

Master of Science (MSc)

Wien | Vienna, 2026

Studienkennzahl lt. Studienblatt | Degree programme code as it appears on the student record sheet:	UA 066 862
Studienrichtung lt. Studienblatt | Degree programme as it appears on the student record sheet:	Masterstudium Chemie
Betreut von | Supervisor:	Univ.-Prof. Dr. Dr. h.c. Leticia Gonzalez Herrero

Acknowledgments

First and foremost, I would like to express my sincere gratitude to my family for their constant support and encouragement. Without them, the academic career I am pursuing and the achievements I have reached so far would not have been possible.

I am deeply grateful to Prof. Leticia González and Prof. Davide Bonifazi for their guidance throughout the past years, for their continuous motivation and confidence in me and for their invaluable advice. I greatly appreciate the opportunity to have worked with them.

I would like to extend my sincere thanks to thank Dr. Johannes Dietschreit and Dr. Pavel Pokhilko for their scientific feedback during my thesis. I am especially grateful for the many scientific discussions that contributed significantly to this thesis.

Furthermore, I would like to thank Dr. Markus Oppel for his support and encouragement since my first semester of studying chemistry. I am also grateful to everyone in the group who made my stay in this group more enjoyable. In particular, I want to acknowledge my colleagues Patrick and Gaurab for the many scientific and informal discussions we shared over the past months.

Abstract

In this thesis, the selective dissociation of S–O and C–O bonds in 2-phenylphenyl triflate is investigated using computational chemistry methods. Motivated by experimental observations, the electrochemically generated radical anion undergoes S-O bond cleavage in the absence of irradiation, as well as under green light (λ' = 523 nm), whereas blue light (λ'' = 405 nm) promotes breaking of the C–O bond. Understanding the mechanism underlying wavelength-selective bond cleavage is important for the rational design of photochemical pathways in organic synthesis under controlled and environmentally friendly conditions. Density functional theory (DFT) calculations reveal that the radical anion is metastable with a positive electron affinity, indicating resonance character. Orbital analysis shows population of a π^* orbital with σ^*(S–O) contribution upon reduction, explaining the experimentally observed S–O bond cleavage in the ground-state. This is further supported by vibrational analysis, where a normal mode corresponding to S–O stretching is identified, while no corresponding mode is found for C–O bond cleavage in the ground-state. Time-dependent density functional theory (TD-DFT), along with complete active space self-consistent field (CASSCF) and subsequent n-electron valence state wave function second-order perturbation theory (NEVPT2) corrections, capture the qualitative nature of the relevant excited states. However, NEVPT2 introduces unusually large and inconsistent energy shifts, highlighting limitations of bound-state methods for this resonance system. To obtain a reliable description, continuum effects were explicitly included using the projected complex absorbing potential-restricted active space configuration interaction (pCAP-RASCI) method, yielding improved agreement with the experimental absorption spectrum. The autodetachment lifetime evaluated with pCAP-RASCI confirms that the radical anion is sufficiently long-lived to undergo photochemical bond cleavage. Overall, the results provide a mechanistic understanding of wavelength-selective bond cleavage and emphasize the importance of explicitly treating electronic resonances.

Kurzfassung

In dieser Arbeit wird die selektive S–O und C–O Bindungsspaltung in 2-phenylphenyl-triflat mittels computergestützter Methoden untersucht. Ausgangspunkt sind experimentelle Beobachtungen, nach denen das elektrochemisch erzeugte Radikalanion ohne Bestrahlung, sowie unter grünem Licht (λ' = 523 nm) die S–O Bindungsspaltung erfolgt, während blaues Licht (λ'' = 405 nm) die Spaltung der C–O Bindung bewirkt. Ziel ist es den zugrundeliegenden Mechanismus dieser wellenlängenselektiven Bindungsspaltung zu verstehen, um photochemische Reaktionen in organischer Synthesechemie gezielt und umweltfreundlich steuern zu können. Berechnungen mit Dichtefunktionaltheorie (DFT) zeigen, dass das intermediäre Radikalanion metastabil ist und eine positive Elektroaffinität aufweist, was auf den Charakter eines elektronischen Resonanzzustantds hindeutet. Orbitalanalysen zeigen die Besetzung eines π^* Orbitals mit σ^*(S–O) Anteil nach elektrochemischer Reduktion des Edukts, was die S–O Bindungsspaltung im Grundzustand erklärt. Schwingungsanalysen zeigen die Präsenz einer S–O Streckmode im Grundzustand, während ein analoger Schwingungsmodus für die C–O Spaltung nicht gefunden wurde. Die angeregten Zustände wurden mittels zeitabhängiger Dichtefunktionaltheorie (TD-DFT), sowie complete active self-consistent field (CASSCF) und anschließender n-electron valence state wave function second-order perturbation theory (NEVPT2) Korrekturen untersucht. NEVPT2 weist jedoch ungewöhnlich große und inkosistente Energieverschiebungen auf, was die Grenzen gebundener Zustandsmethoden für elektronische Resonanzzustände verdeutlicht. Eine verbesserte Beschreibung wird durch die explizite Berücksichtigung von Kontinuumseffekten mittels projected complex absorbing potential-restricted active space configuration interaction (pCAP-RASCI) erreicht, wodurch eine gute Übereinstimmung mit dem experimentellen Absorptionsspektrum erreicht wird. Die berechnete Autodetachmentslebensdauer bestätigt desweiteren, dass das Radikalanion ausreichend langlebig für photochemische Bindungsspaltung ist. Die theoretischen Erkenntnisse geben ein mechanistisches Verständnis der wellenlängenselektiven Bindungsspaltung und unterstreichen die Bedeutung der expliziten Behandlung von Resonanzzuständen.

List of acronyms

CAP	complex absorbing potential
CASSCF	complete active space self-consistent field
CI	configuration interaction
CPCM	conductor-like polarizable continuum model
CT	charge-transfer
DFT	density functional theory
DMSO	dimethylsulfoxide
FC	Franck–Condon
FCI	full configuration interaction
FWHM	full width at half maximum
HF	Hartree–Fock
HOMO	highest occupied molecular orbital
LUMO	lowest unoccupied molecular orbital
MCSCF	multiconfigurational self-consistent field
NEVPT2	n-electron valence state wave function second-order perturbation theory
pCAP	projected complex absorbing potential
PT2	second-order Rayleigh–Schrödinger perturbation theory
RASCI	restricted active space configuration interaction
RASSCF	restricted active space self-consistent field
SA	state-averaged
SC-NEVPT2	strongly contracted n-electron valence state wavefunction second-order perturbation theory

SOMO	singly occupied molecular orbital
TDA	Tamm–Dancoff approximation
TD-DFT	time-dependent density functional theory
TheoDORE	theoretical density, orbital relaxation and exciton analysis
UKS	unrestricted Kohn–Sham formalism

Contents

1. Introduction

The selective transformation of chemical bonds using light has emerged as a promising approach in modern synthetic chemistry.[1] Light irradiation enables the access to electronically excited states that are not reachable under thermal conditions. Photochemical approaches open pathways to enhance selectivity. In particular, controlling reactivity *via* the wavelength of incident light provides a powerful strategy for steering chemical reactions by selectively populating different electronic states.[2] Due to their potential for sustainability and environmentally friendly synthetic routes, wavelength-selective reactivity has gained significant attention.[3] Wavelength-selective bond cleavage represents an opportunity to selectively activate specific bonds within the same molecule by changing the wavelength of the incident light.[4] However, the mechanistic understanding of wavelength-selective chemistry remains limited.[5]

Triflate groups are often used in chemical transformations as they are excellent leaving groups due to the delocalization of the negative charge over the three oxygen atoms.[6,7] Experimental studies conducted by the Bonifazi group[8] from the institute of organic chemistry at the university of Vienna have revealed a wavelength-selective bond cleavage in 2-phenylphenyl triflate (abbreviated as biphenyl triflate in this work; see also structure in the red spectrum in Fig. 1.1). Time-resolved absorption measurements during continuous electrochemical reduction at 2.2 V and light irradiation in dimethylsulfoxide (DMSO) (Fig. 1.1) show the evolution of distinct spectral features during the reaction.

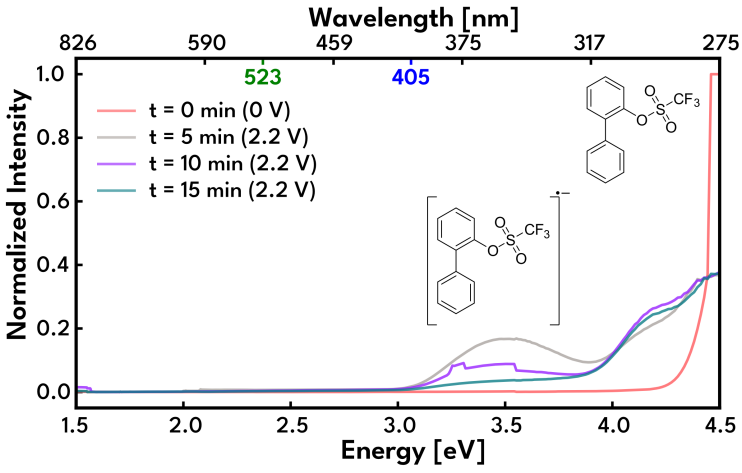

Figure 1.1.: Experimental time-resolved absorption measurements during continuous electrochemical reduction and light irradiation in DMSO. The biphenyl triflate (red) is reduced to a radical anion (gray) with an absorption at around 350 nm which undergoes S–O and C–O bond cleavage.

The initial spectrum of neutral biphenyl triflate, representing the reaction educt prior to electrochemical reduction and light irradiation (red spectrum), shows no significant absorption above 300 nm. After 5 minutes of reaction time, an absorption peak appears at around 350 nm (gray spectrum) representing the radical anion. This peak loses intensity over time (see purple spectrum in Fig. 1.1 after 10 minutes) and disappears completely after 15 minutes (green spectrum). Depending on the wavelength of the incident light used, different products are observed as shown in Fig. 1.2. When using green light (λ' = 523 nm), the S–O bond is cleaved, while blue light (λ'' = 405 nm) induces C–O bond cleavage. Additionally, S–O bond cleavage is observed to occur slowly without irradiation, suggesting a thermally accessible pathway which is accelerated upon excitation.

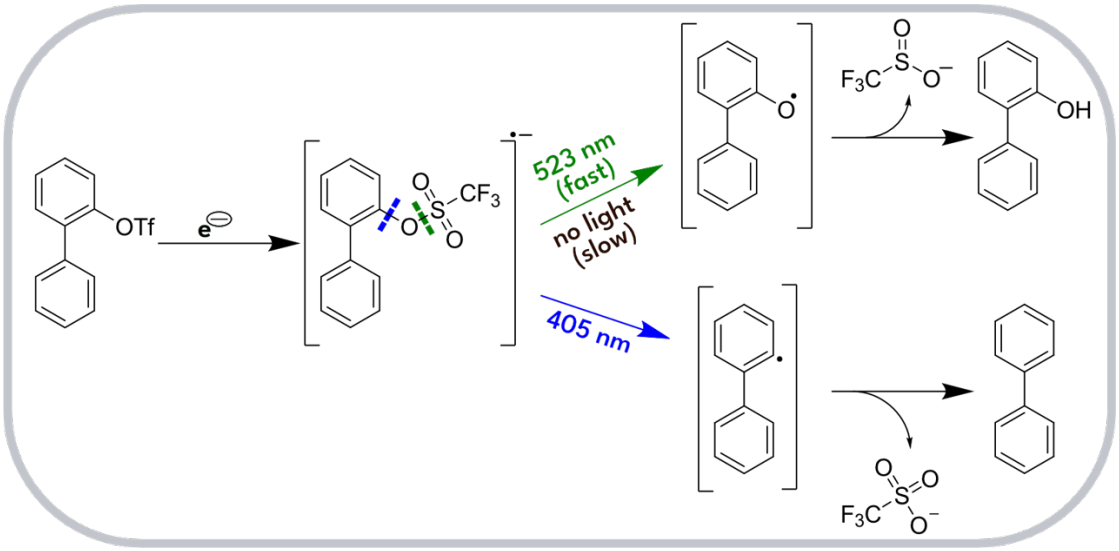

Figure 1.2.: Wavelength-selective S–O and C–O cleavage in biphenyl triflate. Electrochemical reduction of biphenyl triflate generates a radical anion undergoing S–O bond cleavage in the ground state. This process can be accelerated in the excited state upon irradiation at λ' = 523 nm. Using λ'' = 405 nm instead induces C–O bond cleavage. The reaction is performed in DMSO and carried out under continuous electrochemical reduction and simultaneous irradiation. The triflate group is abbreviated with OTf.

In the case of S–O bond cleavage, an oxygen-centered radical is formed with a triflyl anion group as a side product. In contrast, a carbon-centered radical and a triflate anion are the products of the C–O bond cleavage. These two radicals undergo hydrogen atom abstraction, likely from the solvent, leading to the formation of 2-phenylphenol and biphenyl, respectively. Fundamentally different mechanisms are expected for the two cleavages as the C–O bond cleavage is exclusively photoinduced.

These experimental observations raise several questions regarding the nature of the electrochemically generated radical anion and the mechanism behind the wavelength-selective bond cleavage. Radical anions often feature electronic resonance states which are bound states that are embedded into an unbound continuum. Resonances have a finite lifetime due to their

instability towards the loss of an electron. Thus, special theoretical methods are needed to properly describe such resonance states.[9,10] This thesis investigates the wavelength-selective chemistry in biphenyl triflate radical anion using quantum mechanical methods and will include an analysis of both the ground and excited states. Additionally, the two dissociation pathways are explored to gain first insights into the excited state mechanism. The theoretical results obtained within this work are compared with experimental data to establish a mechanistic understanding of the wavelength-selective bond cleavage in triflate-based organic compounds.

These experimental observations raise several questions regarding the nature of the electrochemically generated radical anion and the mechanism behind the wavelength-selective bond cleavage. Radical anions often feature electronic resonance states which are bound states that are embedded into an unbound continuum. Resonances have a finite lifetime due to their instability towards the loss of an electron. Thus, special theoretical methods are needed to properly describe such resonance states.[9,10]

First, the ground-state electronic structures of the neutral and radical anion biphenyl triflate species are analyzed, including their relative stability and orbital character. Subsequently, the excited states and absorption properties of the radical anion are characterized using conventional electronic structure methods designed for bound states. Additionally, the metastable nature of the radical anion is treated explicitly. Electronic resonance states are identified and their autodetachment lifetimes are extracted. Finally, a state correlation diagram is constructed to obtain first mechanistic insights into the S–O and C–O bond cleavage pathways. The results obtained in this thesis aim to improve the understanding in the wavelength-selective chemistry observed in biphenyl triflate.

2. Theoretical Background

This chapter provides an overview of the theoretical foundations of the methods employed in this work. First, a brief introduction to quantum chemistry, including the Schrödinger equation and the Born–Oppenheimer approximation, is given. Subsequently, multiconfigurational wave function-based electronic structure methods are introduced, with particular emphasis on the complete active space self-consistent field (CASSCF) method and n-electron valence state wave function second-order perturbation theory (NEVPT2). Next, both the time-independent and time-dependent formulations of density functional theory (DFT) are discussed. Finally, the last section focuses on electronic resonances and their computational treatment.

2.1. Introduction to Quantum Chemistry

One of the main goals of quantum chemistry is to accurately model quantum systems using the Schrödinger equation. The time-dependent Schrödinger equation is

$$\hat{H}(\mathbf{r},\mathbf{R})\Psi(\mathbf{r},\mathbf{R},t) = i\frac{\partial}{\partial t}\Psi(\mathbf{r},\mathbf{R},t), \tag{1}$$

where $\hat{H}(\mathbf{r},\mathbf{R})$ denotes the Hamiltonian and $\Psi(\mathbf{r},\mathbf{R},t)$ is the time-dependent wave function describing the quantum state of the system. The wave function depends on the position of all electrons $\mathbf{r}$ and nuclei $\mathbf{R}$ and on the time t. Herein, $\mathbf{r} = (\vec{r}_i, \vec{r}_j, ..., \vec{r}_N)$ and $\mathbf{R} = (\vec{R}_A, \vec{R}_B, ..., \vec{R}_M)$ denote the sets of all electronic and nuclear coordinates, respectively. The Hamiltonian $\hat{H}(\mathbf{r},\mathbf{R})$ is associated with the total energy of the many-body system. The explicit form of the non-relativistic Hamiltonian $\hat{H}(\mathbf{r},\mathbf{R})$ without external fields is

$$\begin{aligned}\hat{H}(\mathbf{r},\mathbf{R}) = &\underbrace{-\frac{1}{2}\sum_{i=1}^{N}\nabla_i^2}_{\hat{T}_\mathrm{e}} \underbrace{-\sum_{A=1}^{M}\frac{1}{2M_A}\nabla_A^2}_{\hat{T}_\mathrm{N}} + \underbrace{\sum_{i=1}^{N}\sum_{j>i}^{N}\frac{1}{|\vec{r}_i-\vec{r}_j|}}_{\hat{V}_\mathrm{ee}} \\ &\underbrace{-\sum_{i=1}^{N}\sum_{A=1}^{M}\frac{Z_A}{|\vec{r}_i-\vec{R}_A|}}_{\hat{V}_\mathrm{Ne}} + \underbrace{\sum_{A=1}^{M}\sum_{B>A}^{M}\frac{Z_A Z_B}{|\vec{R}_A-\vec{R}_B|}}_{\hat{V}_\mathrm{NN}},\end{aligned} \tag{2}$$

where small letters enumerate electrons and capital letter nuclei, M_A and Z_A are the mass and the charge of the nuclei. The Hamilton operator $\hat{H}(\mathbf{r},\mathbf{R})$ consists of the kinetic energy of the electrons and nuclei ($\hat{T}_\mathrm{e}$ and $\hat{T}_\mathrm{N}$) and the potential energy terms describing interactions between particles. The potential energy terms depend only on interparticle distances $|\vec{r}_i-\vec{r}_j|$, $|\vec{r}_i-\vec{R}_A|$, and $|\vec{R}_A-\vec{R}_B|$ for the electron–electron repulsion ($\hat{V}_\mathrm{ee}$), the nucleus-electron attraction ($\hat{V}_\mathrm{Ne}$), and the nucleus-nucleus repulsion ($\hat{V}_\mathrm{NN}$), respectively.

For time-independent Hamiltonians, $\Psi(\mathbf{r}, \mathbf{R}, t)$ can be separated into spatial and time-dependent parts, yielding the time-independent Schrödinger equation depending only on the spatial coordinates of electrons and nuclei

$$\hat{H}(\mathbf{r}, \mathbf{R})\Psi(\mathbf{r}, \mathbf{R}) = E\Psi(\mathbf{r}, \mathbf{R}), \tag{3}$$

where $\Psi(\mathbf{r}, \mathbf{R})$ is the time-independent wave function and E is the total energy of the system.[11]

As solving Eq. 3 for polyatomic molecular systems is very challenging, reasonable approximations are needed. One of the most widely used approximations is the Born–Oppenheimer approximation.[12] Born and Oppenheimer showed that treating the nuclei separately from the electrons is a valid approach as nuclei are much heavier than electrons. Within this framework, the motion of nuclei is neglected on the timescale of the electrons.[13] The action of $\hat{T}_\mathrm{N}$ in Eq. (2) on the electronic wave function is neglected leading to a decoupling of electronic and nuclear motions which allows solving the electronic Schrödinger equation for fixed nuclear positions. Thus, the resulting electronic Hamiltonian $\hat{H}_\mathrm{el}$ is defined as

$$\hat{H}_\mathrm{el} = \hat{T}_\mathrm{e} + \hat{V}_\mathrm{ee} + \hat{V}_\mathrm{Ne}. \tag{4}$$

When substituting $\hat{H}_\mathrm{el}$ into Eq. (3), one obtains the time-independent electronic Schrödinger equation

$$\hat{H}_\mathrm{el}(\mathbf{r}; \mathbf{R})\Psi_\mathrm{el}(\mathbf{r}; \mathbf{R}) = E_\mathrm{el}(\mathbf{R})\Psi_\mathrm{el}(\mathbf{r}; \mathbf{R}), \tag{5}$$

where Ψ_el is the electronic wave function, E_el the electronic energy which is given by $E - V_\mathrm{NN}$ and $\mathbf{R}$ is now a parameter. Ψ_el depends explicitly on the electronic coordinates and parametrically on the nuclear coordinates. The electronic Schrödinger equation can be solved for each nuclear configuration yielding a potential energy surface.[12,13]

One of the simplest approaches to approximately solve Eq. (5) is the Hartree–Fock (HF) method, in which the many-electron wave function is represented by a single Slater determinant Θ. A Slater determinant is an antisymmetrized product of N one-electron wavefunctions $\varphi_i(\vec{x})$[13]

$$\Theta = \frac{1}{\sqrt{N!}} \begin{vmatrix} \varphi_1(\vec{x}_1) & \varphi_2(\vec{x}_1) & \cdots & \varphi_N(\vec{x}_1) \\ \varphi_1(\vec{x}_2) & \varphi_2(\vec{x}_2) & \cdots & \varphi_N(\vec{x}_2) \\ \vdots & \vdots & \ddots & \vdots \\ \varphi_1(\vec{x}_N) & \varphi_2(\vec{x}_N) & \cdots & \varphi_N(\vec{x}_N) \end{vmatrix}, \tag{6}$$

where $\vec{x}$ summarizes spatial and spin coordinates. This form ensures the antisymmetry of the wave function with respect to the exchange of two electrons. The orbitals are optimized variationally to yield the lowest possible energy within the space of single-determinant wave functions. The total energy is obtained as the expectation value of $\hat{H}_\mathrm{el}$ with respect to Θ. Herein, the electron–electron interaction energy can be decomposed into a Coulomb term describing electron–electron repulsion and an additional exchange contribution. The exchange contribution arises from the fact that electrons with the same spin avoid each other due to Pauli repulsion. In HF, this exchange is treated exactly within the single-determinant framework, while electron correlation is neglected. Electron correlation describes the additional instantaneous adjustment of electron motion beyond the average Coulomb interaction.[13]

2.2. Multiconfigurational Realm in Theoretical Chemistry

The exact non-relativistic electronic wave function can be expressed within the full configuration interaction (FCI) framework as a linear combination of all possible Slater determinants as

$$\Psi_{\mathsf{FCI}} = \sum_i c_i \Theta_i, \tag{7}$$

where the expansion coefficients c_i determine the weight of each configuration and Θ_i denotes a Slater determinant. As all possible electron configurations are considered in FCI, the number of Θ included in Ψ_{FCI} grows combinatorially and therefore exponentially with system size. Although FCI is computationally unfeasible for most chemical systems, the structure of the FCI wave functions can aid the design of efficient approximations. The magnitude of c_i determines the regime of the electron correlation. If a single determinant (typically the HF determinant Ψ_{HF}) is the only leading configuration and the weights of all other determinants are small, an approximation of the FCI wave function in terms of the single determinant is qualitatively correct. Determinants with small weights contribute to the weak (dynamic) electron correlation. If several determinants have substantial weights, the single-determinant approximation is qualitatively incorrect. In this case, the electron correlation is strong (static).

The wave-function methods targeting treatment of the weak electron correlation are based on the expansions around the HF determinant. For example, truncating configuration interaction (CI) up to the excitations of a certain rank (e.g., CISD — CI singles and doubles) gives a hierarchy the systematically improvable approximations toward FCI. Such methods are designed for systems which are qualitatively correctly described by a single determinant but may fail in the presence of significant static correlation.

2.2.1. Complete Active Space Self-Consistent Field (CASSCF)

The multireference strategy is based on the assumption that there are several main contributors to the FCI wave function. For example, within the multiconfigurational self-consistent field (MCSCF) method, a variational optimization of the weights of such determinants is combined with the variational optimization of orbitals. The most common variant of MCSCF is the CASSCF method that considers all possible determinants constructed within a small subset of orbitals called active orbitals. The remaining orbitals form inactive (doubly occupied) and virtual (empty) orbital spaces. When choosing the active space one needs to consider the chemical problem and the computational cost. Ideally, the active space should contain all orbitals which are relevant when exploring the potential energy surface. While no strict protocol exists for finding a suitable active space, the following rules can guide the selection process:

1. Orbitals that are involved in the chemical process of interest, such as a σ^* orbital associated with bond dissociation, have to be included in the active space to ensure a proper description of the underlying electronic structure changes.

2. Natural orbitals with fractional occupation numbers significantly different from 0 and 2 often indicate orbitals that are contributing significantly to the multiconfigurational character of the wave function.

3. The active space is often refined iteratively by starting from an initial guess and updating the orbital selection based on the results of previous calculations.

Once a suitable active space is selected, the orbitals can be optimized in two different ways over different electronic states. In a state-specific CASSCF setting, the orbitals are optimized for a single electronic state at a time, yielding an accurate description of that single electronic state. However, electronic states that are close in energy can be difficult to optimize in state-specific CASSCF due to root flipping (i.e., changes in the ordering and character of the electronic states during the orbital optimization procedure). Furthermore, computing properties involving multiple states is complicated in a state-specific framework as each state is represented by its own generally non-orthogonal set of orbitals.

To describe several electronic states which are close in energy, the state-averaged (SA) orbital optimization is introduced. The SA CASSCF[14] framework considers an orbital optimization of the objective function, which is the weighted-average of the total energies of the selected electronic states defined as[14,15]

$$E = \sum_x w_x E_x, \tag{8}$$

where $\sum_x w_x = 1$. The weights w_x are defined by the user and control the relative importance of each state. In many cases, equal weights are used and the electronic states are described by using a common orbital set to obtain a democratic description of all states. This facilitates the calculation of transition dipole moments as the wave functions of different states are expressed in the same orbital basis, enabling a direct evaluation of the transition dipole moment.[15]

Due to its formulation, CASSCF still inherits the exponential scaling of FCI within the active space. Consequently, CASSCF becomes unfeasible for large active spaces.[15] Malmqvist, Alistair and Roos introduced the restricted active space self-consistent field (RASSCF) method to address the computational cost of CASSCF.[16] In RASSCF, the active space is further split into three subspaces labeled as RAS 1, RAS 2 and RAS 3, which have different constraints (see also Fig. 2.1 for a comparison of CASSCF and RASSCF). While the RAS 2 space corresponds to the active space in CASSCF, the RAS 1 and RAS 3 spaces consider a controlled restriction of excitations. The RAS 1 space consists of mainly doubly occupied orbitals from which only a limited number of electron holes are allowed while RAS 3 consists of unoccupied orbitals to which only a limited number of electrons are excited.[15,16]

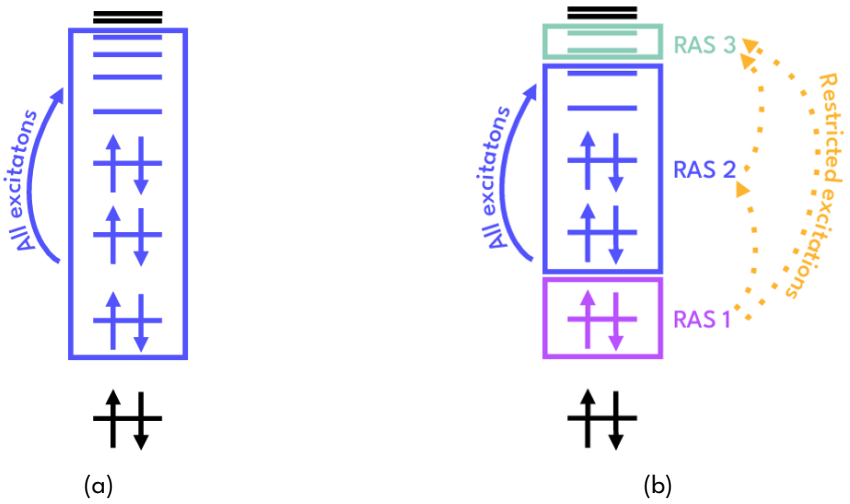

Figure 2.1.: Schematic representation of orbital partitions in **(a)** CASSCF and **(b)** RASSCF.

Naturally, the restricted active space approach can also be used within the CI framework without optimizing the orbitals, known as restricted active space configuration interaction (RASCI). It is therefore possible to further reduce computational cost and treat larger active spaces, at the expense of less accurate orbital representations.

2.2.2. N-Electron Valence State Perturbation Theory (NEVPT2)

While CASSCF accounts for the static electron correlation within a predefined active space, it does not capture the dynamic correlation well that comes from numerous other determinants with small weights. A common strategy to include the dynamic correlation on top of CASSCF is based on perturbation theory. In second-order Rayleigh–Schrödinger perturbation theory (PT2), the energy is expanded up to the second-order in the perturbation, which yields a correction to the reference energy. Within PT2, the electronic Hamiltonian is given by a solvable zeroth-order Hamiltonian $\hat{H}_0$ and a perturbation $\hat{V}$. Formally, $\hat{H}_{\text{PT2}}$ is expressed as

$$\hat{H}_{\text{PT2}} = \hat{H}_0 + \hat{V}, \tag{9}$$

where $|\Psi_0\rangle$ is an eigenfunction of $\hat{H}_0$ and the perturbation $\hat{V}$ is defined as $\hat{H}_{\text{el}} - \hat{H}_0$. Depending on the choice of $\hat{H}_0$, excitations outside the reference active space are generated. Expanding the wave function by the orders of $\hat{V}$ and projecting onto the external states gives rise to perturbative corrections for the wave function. Inserting these corrections into the energy expectation value yields the second-order PT2 correction to the energy $E^{(2)}$

$$E^{(2)} = \sum_{\text{ext}} \frac{|\langle \Psi_0 | \hat{V} | \varphi_{\text{ext}} \rangle|^2}{E^{(0)} - E^{(0)}_{\text{ext}}}, \tag{10}$$

where ext indexes external states, defined as configurations involving excitations outside the active space. This PT2 correction corrects for dynamic correlation by summing up over energy

contributions from the high-energy excitations. When $E_{\text{ext}}^{(0)}$ becomes close to the reference energy $E^{(0)}$, the energy denominator in Eq. (10) becomes small, leading to large second-order energy corrections. Such external states are called intruder states. The NEVPT2 method is designed to avoid intruder states by construction.

Different definitions of $\hat{H}_0$ yield different variants of perturbation theory. The main idea of NEVPT2 is to construct $\hat{H}_0$ in such a way that the multiconfigurational character of the CASSCF reference wave function is preserved and that active orbitals are treated equally in both the reference and perturbed space. The Dyall Hamiltonian $\hat{H}_0^{\mathsf{D}}$ fulfills these criteria and is defined as

$$\hat{H}_0^{\mathsf{D}} = \hat{H}_{\mathsf{i}}^{\mathsf{D}} + \hat{H}_{\mathsf{v}}^{\mathsf{D}}, \tag{11}$$

where $\hat{H}_{\mathsf{i}}^{\mathsf{D}}$ is a mean-field one-electron Hamiltonian acting on the inactive and virtual orbitals and $\hat{H}_{\mathsf{v}}^{\mathsf{D}}$ is the Hamiltonian within the active space explicitly describing the electron–electron Coulomb repulsion. The choice of the zeroth-order Hamiltonian in NEVPT2 preserves the multiconfigurational character of the reference wave function and leads to a balanced description of the reference and external space. One key advantage of NEVPT2 is its intruder-state-free construction, since the excitation energies entering the second-order denominator are defined so that vanishing denominators are avoided.[17]

In practice, different implementations of NEVPT2 arise from how the external space is treated. The most commonly used approach is strongly contracted n-electron valence state wavefunction second-order perturbation theory (SC-NEVPT2), in which all configurations belonging to a given excitation class are combined into a single effective perturber. This results in a computationally efficient method while still providing a reliable and accurate description of dynamic correlation.[17]

2.3. Density Functional Theory (DFT)

The electronic wave function is a complicated object that depends on the coordinates and spins of all the electrons. The dependence on the degrees of freedom of all the electrons inevitably leads to bulky tensor products of one–electron functions and a high computational cost even for approximate wave-function electronic structure methods. The electron density $\rho(\vec{r})$ depends only on three spatial coordinates instead of the coordinates of multiple electrons and is experimentally observable.[13] The electron density $\rho(\vec{r})$ is defined as

$$\rho(\vec{r}) = N \int \dots \int |\Psi(\vec{x}_1, \vec{x}_2, \dots, \vec{x}_N)|^2 \mathrm{d}s_1 d\vec{x}_2 \dots \mathrm{d}\vec{x}_N. \tag{12}$$

The electron density $\rho(\vec{r})$ is the probability of finding one of the N electrons in a volume element, regardless of the spin. The other $N-1$ electrons possess arbitrary positions and spins. Powerful theorems connect the electron density with certain observables, providing recipes for a simpler (and often cheaper) computational description of a quantum system based only on $\rho(\vec{r})$.

2.3.1. The Hohenberg-Kohn theorems

The first Hohenberg–Kohn theorem states that the ground-state electron density $\rho_0(\vec{r})$ determines the external potential $v_{\text{ext}}(\vec{r})$ [18,19]

$$v_{\text{ext}}(\vec{r}) = v_{\text{ext}}[\rho_0](\vec{r}). \tag{13}$$

This external potential is usually defined as the electron–nucleus Coulomb attraction ($\hat{V}_{\text{Ne}}$) for molecules within the Born–Oppenheimer approximation

$$\hat{V}_{\text{Ne}} \equiv \hat{V}_{\text{ext}} = \sum_i v_{\text{ext}}(\vec{r}_i), \tag{14}$$

where the electron coordinate is r_i and Z_A the nuclear charge at position R_A. $\hat{V}_{\text{ext}}(\vec{r})$ is chosen in such a way that the electron-density of the non-interacting system is the same as the electron density of the interacting system.[18] If the electronic Hamiltonian $\hat{H}_{\text{el}}$ (see Eq. (4)) depends on $\hat{V}_{\text{ext}}(\vec{r})$, the ground-state electron density is uniquely determined by the ground-state wave function via a functional. The ground-state energy $E_0[\rho_0]$ is

$$E_0[\rho_0] = T[\rho_0] + E_{\text{ee}}[\rho_0] + E_{\text{Ne}}[\rho_0]. \tag{15}$$

where the functional form of $T[\rho_0]+E_{\text{ee}}[\rho_0]$ is independent of the system (universal functionals). $E_{\text{Ne}}[\rho_0]$ on the contrary explicitly depends on the system. The system-independent part in Eq. (15) is summarized in the Hohenberg–Kohn functional $F_{\text{HK}}[\rho_0]$. When applying an arbitrary $F_{\text{HK}}[\rho_0]$ to the electron density, one obtains

$$F_{\text{HK}}[\rho] = T[\rho] + E_{\text{ee}}[\rho] = \langle\Psi|\,\hat{T} + \hat{V}_{\text{ee}}\,|\Psi\rangle\,, \tag{16}$$

where the expectation value $\langle\Psi|\,\hat{T} + \hat{V}_{\text{ee}}\,|\Psi\rangle$ is the sum of the kinetic energy of the electrons and their repulsion in state Ψ. Thus, $F_{\text{HK}}[\rho]$ replaces the many-body wave function problem. However, the exact form of $F_{\text{HK}}[\rho]$ is in general not known.[13]

The second Hohenberg–Kohn theorem states that $F_{\text{HK}}[\rho]$ will yield the lowest energy if the input density $\rho(\vec{r})$ resembles the true ground state density $\rho_0(\vec{r})$. Any deviation from $\rho_0(\vec{r})$ will result in higher energies. Thus, the second Hohenberg–Kohn theorem introduces a variational principle for DFT.[13,19]

2.3.2. The Kohn-Sham approach

In 1965, Kohn and Sham introduced a way for computing $\rho(\vec{r})$ and consequently the total energy of a many-electron system.[20] Kohn and Sham proposed a non–interacting reference system constructed in such a way that its electron density matches the electron density of a real system. The wave function of the non-interacting reference system consisting of N electrons can be represented by a Slater determinant. Within the Kohn–Sham framework, $\varphi_i(\vec{x})$ in Eq. (6) are the Kohn–Sham spin-orbitals. By construction, this Slater determinant reproduces the ground-state electron density of the real system

$$\rho_0(\vec{r}) = \sum_i^N \sum_s |\varphi_i(\vec{x})|^2. \tag{17}$$

The main idea of Kohn and Sham was to calculate the kinetic energy as accurately as possible, since the exact evaluation is not possible. They separated the functional into the terms which could be calculated exactly: the kinetic energy of the artificial system $T_s[\rho(\vec{r})]$ and the Coulomb interactions $J[\rho(\vec{r})]$. Kohn and Sham summarized all terms which cannot be calculated exactly into a third term, the exchange correlation functional E_{XC} which is given by[13]

$$E_{XC}[\rho(\vec{r})] = (\hat{T}[\rho(\vec{r})] - \hat{T}_s[\rho(\vec{r})]) + (\hat{V}_{ee}[\rho(\vec{r})] - J[\rho(\vec{r})]). \tag{18}$$

By combining all these terms the general functional in DFT becomes[13]

$$F[\rho(\vec{r})] = T_s[\rho(\vec{r})] + J[\rho(\vec{r})] + E_{XC}[\rho(\vec{r})]. \tag{19}$$

As an explicit and practically usable form of E_{XC} is not known, different approximate functionals for E_{XC} have been formulated.[13,20] One of the earliest approaches to approximate E_{XC} is the local density approximation, in which the density is locally approximated as a uniform gas. Thus, the exchange-correlation energy depends only on $\rho(\vec{r})$.[15] The generalized gradient approximation improves upon these functionals to account for the inhomogeneous nature of molecules. Herein, not only the electron density but also the gradient of $\rho(\vec{r})$ is included. Including higher-order derivatives of $\rho(\vec{r})$ leads to improved meta-generalized gradient approximation functionals enabling more flexibility of the functional.[15]

An improvement in DFT functionals was introduced by hybrid functionals like B3LYP[21,22] which include a fraction of exact Fock exchange. Hybrid functionals reduce the self-interaction errors arising from approximate density functionals.[15]

Range-separated hybrid functionals were developed to address the incorrect long-range behavior of the exchange-correlation functional. Within such functionals, the electron–electron interaction terms are split into short- and long-range contributions. The short-range exchange is treated with DFT exchange, including a fraction of HF exchange, while the long-range part uses 100% Fock exchange.[15] The ωB97X-D3 functional used in this work incorporates 22% short-range HF exchange and includes the third generation Grimme dispersion correction (D3).[23]

The formalism presented until now was initially only designed for closed-shell systems. However, in an open-shell system, where the number of electrons is odd, the core variable in the context of DFT still remains the total electron density. If the number of α and β electrons is unequal, the total electron density is given by

$$\rho(\vec{r}) = \rho_\alpha(\vec{r}) + \rho_\beta(\vec{r}), \tag{20}$$

In the unrestricted Kohn–Sham formalism (UKS) formalism, the restriction that pairs of α and β electrons occupy the same spatial orbital is lifted. As the α and β orbitals are optimized independently, their spatial parts may differ. It is important to note that the Slater determinant Θ constructed from the Kohn–Sham orbitals is generally not an eigenfunction of the spin-operator $\hat{S}^2$. The expectation value of $\langle \hat{S}^2 \rangle$ might deviate from the ideal spin value for UKS solutions. This deviation is often used as an indicator of spin-symmetry breakage in an UKS calculation and is called spin contamination.[13,24,25]

2.3.3. Time-Dependent Density Functional Theory (TD-DFT)

The DFT formalism presented above describes only the ground-state electron density. For excited states, time-dependent density functional theory (TD-DFT) which is based on the Runge–Gross[26] and van Leeuwen[27] theorems, employs the time-dependent Kohn–Sham equation. The first Runge–Gross theorem states that the time-dependent electron density $\rho(\vec{r},t)$ is a functional of an external potential $\hat{V}_{\text{ext}}(\vec{r},t)$

$$\rho(\vec{r},t) = \rho[\hat{V}_{\text{ext}}(\vec{r},t)](\vec{r},t). \tag{21}$$

where $\hat{V}_{\text{ext}}(\vec{r},t)$ is chosen in such a way that the time-dependent electron density of the non-interacting system is equal to the the time-dependent electron density of the interacting system.[26,28]

TD-DFT is usually employed with linear-response theory where the response of $\rho(\vec{r},t)$ to a time-dependent electric field is simulated. Excitation energies and oscillator strengths can be calculated from the resulting oscillations in $\rho(\vec{r},t)$. Thus, linear-response TD-DFT is widely used in computational photochemistry. Within the linear response TD-DFT framework, the excitation energies ω are obtained by solving the Casida equation

$$\begin{pmatrix} A(\omega) & B(\omega) \\ -B^*(\omega) & -A^*(\omega) \end{pmatrix} \begin{pmatrix} X(\omega) \\ Y(\omega) \end{pmatrix} = \omega \begin{pmatrix} X(\omega) \\ Y(\omega) \end{pmatrix}, \tag{22}$$

where the matrices A and B describe the coupling between electronic excitations and are constructed from Kohn–Sham orbital energy differences, while the excitation and de-excitation amplitudes are given by X and Y, respectively.[28,29] Eq. (22) can be simplified into an eigenvalue problem by the Tamm–Dancoff approximation (TDA) which neglects the de-excitation amplitudes

$$AX = \omega X. \tag{23}$$

The TDA offers a way to reduce computational cost of TD-DFT calculations and often improves their numerical stability.[29–31]

2.4. Resonances and Non-Hermitian Quantum Mechanics

2.4.1. Electronic Resonance States

Electronic resonance states are bound states which are embedded in the unbound continuum and are unstable towards the loss of an electron, also known as autodetachment. An anion is stable only if the electron affinity EA between the neutral and anion species

$$EA = E_{\text{anion}} - E_{\text{neutral}}, \tag{24}$$

is negative.[10] If the electron affinity is positive, a metastable anion with a finite lifetime is formed. As electronic resonances decay over time, the electron escapes to infinity. Such wave functions are not L^2 integrable.

Standard electronic structure methods are designed only for bound electronic states. Although these methods can fail to properly describe electronic resonances, they may still provide

an approximate position and the character of the resonance states when compact basis sets lacking sufficiently diffuse functions are used, stabilizing the resonance state. However, the continuum, as well as the coupling from the electronic resonance to the continuum cannot be adequately described by such small basis sets. The decay process is therefore not captured and only an approximate energetic ordering and electronic character of the valence resonances are obtained. Capturing the width of the resonances can be more challenging. A common strategy to model resonances is to transform the wave function of a resonance into an L^2 integrable one, which makes it describable by standard electronic structure methods developed for bound states. Among the family of such transformations, one of the most successful is the transformation into the non-Hermitian Hamiltonians[9]. Within the non-Hermitian picture, resonances can be represented in the Siegert representation[32] which describe states with finite lifetime

$$E_{\text{tot}} = E_{\text{R}} - i\frac{\Gamma}{2}, \tag{25}$$

where E_{tot} is the total energy of the resonance, E_{R} the real part of the resonance energy and Γ the decay width of the resonance which determines the autodetachment lifetime of an electronic resonance state.

2.4.2. Complex Absorbing Potential (CAP)

One of the most commonly used non-Hermitian approaches is the complex absorbing potential (CAP) method. CAP makes the wave function of resonances L^2 integrable by absorbing the non-integrable tail of the wave function. The CAP-augmented Hamiltonian $\hat{H}^{\text{CAP}}(\eta)$ is

$$\hat{H}^{\text{CAP}}(\eta) = \hat{H}_{\text{el}} - i\eta\hat{W}, \tag{26}$$

where $\hat{H}_{\text{el}}$ is the electronic Hamiltonian, η is the CAP strength, and $\hat{W}$ is the absorbing potential.[9,33] In the simplest definition of $\hat{W}$, the molecule is entrapped in a box, where a parabolic CAP is applied starting at the boundaries of the box. Although this approach is effective for small molecules, it becomes less suitable for larger, highly asymmetric structures, such as the system studied here. In this work, Voronoi isosurfaces[34] are used as they wrap around the molecule, utilizing space efficiently and preserving the molecular symmetry. The Voronoi absorbing potential $\hat{W}^V$ is

$$\hat{W}^V(\vec{r}) = \begin{cases} 0 & r_{\text{nearest}} \leq r_{\text{cut}} \\ (r_{\text{nearest}} - r_{\text{cut}})^2 & r_{\text{nearest}} > r_{\text{cut}} \end{cases}, \tag{27}$$

where the distance to the atom in closest proximity $r_{\text{nearest}}(\vec{r})$ is given by positions of nuclei $\vec{R}_A$ as

$$r_{\text{nearest}}(\vec{r}) = \min_A(|\vec{r} - \vec{R}_A|). \tag{28}$$

The cutoff radius r_{cut} of the Voronoi potential controls the spatial onset of the absorbing potential. Thus, r_{cut} has to be chosen in such a way that it is large enough that the CAP vanishes in the region where the bound part of the wave function is localized to avoid artifacts. On the

other hand, r_{cut} needs to be small enough that the CAP is applied before the ejecting electron reaches the boundary of the finite basis set representation to avoid reflection from the basis set edges. An optimal r_{cut} value is typically chosen where CAP eigenvalue trajectories (the eigenvalues of $\hat{H}^{\text{CAP}}(\eta)$ for a series of η values) are stable and the resonance position and width show only minimal dependence on r_{cut}.

The above introduced variant of the Voronoi isosurfaces is not continuously differentiable at the region where the Voronoi cells are connected. As the absorbing potential has sharp edges at the boundary regions, the electron is not smoothly absorbed but reflected back. However, this effect is expected to be negligible as $\hat{W}^V$ is represented in a Gaussian basis which cannot fully resolve such sharp discontinuities. The smooth Voronoi which is also used in this work CAP solves this problem. In the smooth Voronoi CAP, the distance to the molecule r_{smooth} is given by a weighted average of the distances of the nuclei as

$$r_{\text{smooth}}(\vec{r}) = \sqrt{\frac{\Sigma_A w_A r_A^2}{\Sigma_A w_A}}, \tag{29}$$

where r_A is the distance to a nucleus A and the weights w_A are further given by

$$w_A = \frac{1}{(r_A^2 - r_{\text{nearest}}^2 + 1.0\ \text{a}_0)^2}. \tag{30}$$

The weights are largest for atoms with distances similar to that of the nearest atom so that only a few narby atoms contribute significantly. The smooth Voronoi CAP $\hat{W}^{\text{SV}}$ is then analogously to Eq. (27) defined as[34]

$$\hat{W}^{\text{SV}}(\vec{r}) = \begin{cases} 0 & r_{\text{smooth}} \leq r_{\text{cut}} \\ (r_{\text{smooth}} - r_{\text{cut}})^2 & r_{\text{smooth}} > r_{\text{cut}} \end{cases}, \tag{31}$$

To determine the CAP strength η, the complex eigenvalues E_{CAP} of $\hat{H}^{\text{CAP}}(\eta)$ are calculated for a series of η. The eigenvalues of the CAP Hamiltonian change the least at the optimal η value which is given by

$$\eta_{\text{opt}} = \arg\min_{\eta} \left| \eta \frac{dE_{\text{CAP}}(\eta)}{d\eta} \right|. \tag{32}$$

Thus, in the original CAP formalism, each η point of the η trajectories requires an electronic structure calculation.[34] Just determining η_{opt} can therefore become very expensive. The projected complex absorbing potential (pCAP) method addresses this issue by using a state-interaction approach in a subset of states.[35] Within this framework, a subset of electronic states $|\Phi_i\rangle, |\Phi_j\rangle, \ldots, |\Phi_N\rangle$ at $\eta = 0$ is obtained first with any suitable electronic structure method. Subsequently, the CAP is added only to this subspace of states. The CAP operator is then expressed as a matrix $\hat{W}^{\text{pCAP}}$ in the basis of the subspace as

$$\hat{W}^{pCAP} = \begin{pmatrix} \langle\Phi_1|\hat{W}|\Phi_1\rangle & \langle\Phi_1|\hat{W}|\Phi_2\rangle & \cdots & \langle\Phi_1|\hat{W}|\Phi_N\rangle \\ \langle\Phi_2|\hat{W}|\Phi_1\rangle & \langle\Phi_2|\hat{W}|\Phi_2\rangle & \cdots & \langle\Phi_2|\hat{W}|\Phi_N\rangle \\ \vdots & \vdots & \ddots & \vdots \\ \langle\Phi_N|\hat{W}|\Phi_1\rangle & \langle\Phi_N|\hat{W}|\Phi_2\rangle & \cdots & \langle\Phi_N|\hat{W}|\Phi_N\rangle \end{pmatrix}, \tag{33}$$

where $\hat{W}$ is the complex absorbing potential given in Eq. 26. Thus, the pCAP Hamiltonian $\hat{H}^{pCAP}(\eta)$ is in analogy to Eq. (26)

$$\hat{H}^{\text{pCAP}}(\eta) = \hat{H}^{0}_{\text{el}} - i\eta\hat{W}^{\text{pCAP}}. \tag{34}$$

As only one electronic structure calculation is required to construct the state-interaction Hamiltonian, pCAP has a large computational advantage over the original CAP. The diagonalization of $\hat{H}^{\text{pCAP}}(\eta)$ yields complex eigenvalues E_{UC}, which are typically referred to as uncorrected CAP energies that depend on η. A finite CAP strength introduces a perturbation of the Hamiltonian, leading to an artificial dependence of the uncorrected energies on η. To address this problem, a first-order correction is usually applied, as proposed by Ref. 36. Herein, the perturbation originating from the finite CAP strength is removed yielding the first-order corrected energies $E^{(1)}_{\text{C}}$

$$E^{(1)}_{\text{C}} = E_{\text{UC}}(\eta) - \eta\frac{dE_{\text{UC}}(\eta)}{d\eta}. \tag{35}$$

This correction improves the stability of extracted resonance positions and widths in respect to η.[9,37]

3. Computational Details

This chapter summarizes the computational details of the electronic structure methods used in this work and is divided into two parts. First, Hermitian electronic structure methods were employed to investigate ground- and excited state properties of the neutral and radical anion biphenyl triflate species. For the ground-state calculations, DFT was used, while the excited states were assessed using TD-DFT and the multiconfigurational methods CASSCF and SC-NEVPT2. Second, the electronic resonance character of the radical anion was treated explicitly using the pCAP formalism in combination with RASCI.

3.1. Hermitian Electronic Structure Calculations

3.1.1. Density Functional Theory

The neutral biphenyl triflate molecule was always calculated as neutral singlet and the radical anion species as a doublet anion. All DFT and TD-DFT calculations were carried out using the Orca 6.1 program package[38] with the restricted Kohn–Sham formalism for closed and UKS formalism for open shell species. Initial molecular structures were generated with RDKit[39] and pre-optimized using the MMFF94[40–44] molecular mechanics force field (for further information see also Lst. A.1 in Appendix A.1.1). Ground state geometries were optimized using the range-separated hybrid functional ωB97X-D3[23,45–47] together with the def2-TZVPD[48,49] basis set. The ωB97X-D3 functional was used as ωB97X-type functionals have shown reliable performance for organic molecules (see Fig. A.1 in Appendix A.1.2 for a comprehensive overview of the performance of different DFT functionals for the biphenyl triflate radical anion).[50] The resolution of identity with chain of spheres (RIJCOSX)[51] approximation was employed in combination with the def2/J auxiliary basis set. Additionally, the tight self-consistent field convergence criteria (TightSCF) was used and the NoTrah flag was activated to achieve easier convergence. Solvent effects were included using the conductor-like polarizable continuum model (CPCM)[52,53] with DMSO as solvent, consistent with experimental conditions. The atomic charges were analyzed using the Hirshfeld population analysis[54] on the DFT optimized ground-state geometry at the unrestricted HF level of theory. Herein, the molecular electron density is partitioned with respect to the electron density contributions of the neutral atoms.

The lowest 30 excited states were calculated at the optimized ground-state geometry with TD-DFT in combination with TDA and the same level of theory used for the DFT optimizations. The excited state characterization was carried out using the theoretical density, orbital relaxation and exciton analysis (TheoDORE)[55] program package. Theoretical absorption spectra were generated using a Gaussian broadening with a full width at half maximum (FWHM) of 0.3 eV.

To analyze normal modes relevant for bond cleavage, the vibrational frequencies of biphenyl triflate radical anion were calculated using the Gaussian 16 program package[56] for better visualization at the UKS ωB97X-D3/def2-TZVPD CPCM(DMSO) level of theory. A FWHM of 10 cm^{-1}

was used for the infrared spectrum.

3.1.2. Multiconfigurational Excited State Calculations

Multiconfigurational calculations were performed using a combination of the HUMboldt Multi-Reference (HUMMR)[57,58] and OpenMOLCAS 23.10[59] programme package. A suitable active space at the Franck–Condon (FC) geometry was determined using the ASS1ST[60–62] protocol which selects orbitals for the active space based on quasi natural orbital occupation numbers obtained from a SC-NEVPT2 calculation. Orbitals with occupation numbers differing significantly from 0 and 2 were classified as strongly correlated and included in the active space. A (9, 9) active space at the FC geometry was identified based on this procedure from SA CASSCF calculations over 10 doublet states using the def2-TZVPD basis set. The FC active space (see Fig. 3.1) consists primarily of π and π^* orbitals localized on the biphenyl moiety.

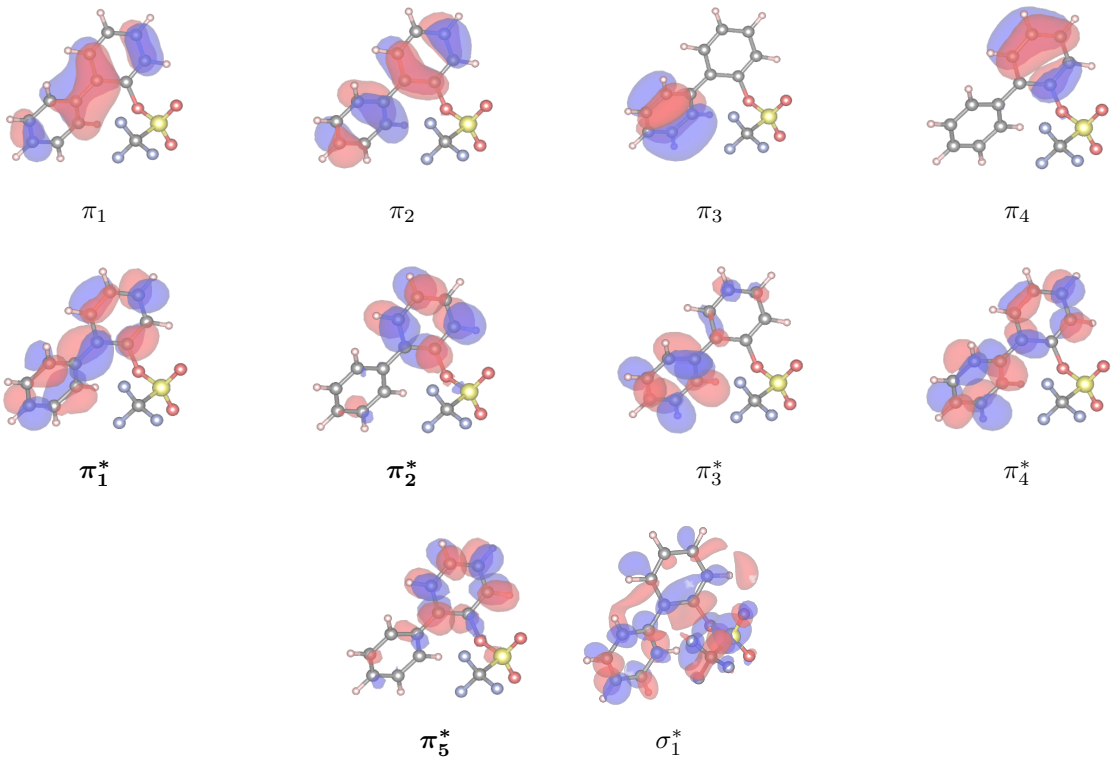

Figure 3.1.: Franck-Condon active space orbitals of the biphenyl triflate radical anion, calculated with $SA_{10}(9, 9)$ CASSCF/def2-TZVPD with ASS1ST protocol. π^* orbitals with σ^*(S–O) contributions, which become apparent when lowering the isovalue (see Fig. A.2 in Appendix A.1.4), are labeled in bold. The σ_1^* orbital with σ^*(C–O) contribution has to be included to describe the C–O bond cleavage. Orbitals are sorted by energy. Molecules are colored by element (C: gray, F: light red, O: dark red and S: yellow).

For simplicity, orbitals with σ^*(S–O) contribution are labeled in bold throughout this work. To identify the states responsible for the excited state bond cleavages, the 9 lowest excited

doublet states were calculated with (9, 9) SA-CASSCF and SC-NEVPT2 with def2-TZVPD and the def2-JK auxiliary basis set, as well as CPCM(DMSO). In order to also describe the C–O bond cleavage, the (9, 9) active space was extended with σ_1^* orbital to yield a (9, 10) active space able to describe both the S–O and C–O bond cleavage. A state correlation diagram was constructed with (9, 10) CASSCF/def2-TZVPD with the DFT optimized FC and dissociated structure (r (S–O) = 10.35 Å and r (C–O) = 10.24 Å, respectively) in OpenMOLCAS. To ensure a common active space for all three structures, the orbitals of the (9, 10) active space were constrained using the SupSYM keyword.

These Hermitian electronic structure methods were used to get a qualitative overview of the S–O and C–O bond cleavage mechanism. In order to get a quantitative description at the FC geometry, pCAP-RASCI was used.

3.2. Explicit Treatment of Resonances with Projected Complex Absorbing Potential-Restricted Active Space Configuration Interaction

To explicitly account for the metastable character of the biphenyl triflate radical anion and its coupling to the continuum states, pCAP calculations were performed in combination with RASCI using OpenMOLCAS interfaced with PyOpenCAP[63]. Additional diffuse basis functions (1s1p1d) were added to the center of mass of the molecule to describe the diffuse continuum states. First, the lowest 29 excited states were calculated with RASCI/def2-TZVPD+1s1p1d at the FC point. The FC active space without π_5^* due to strong orbital mixing was included into RAS 2 and the 20 lowest lying diffuse orbitals were included in RAS 3, while RAS 1 was left empty. Single excitations were allowed into RAS 3. The solvent was excluded to avoid artificial stabilization of continuum.

The RASCI state energies ($E_{D_i}^{\text{RASCI}}$) were used as diagonal elements for the electronic Hamiltonian $\hat{H}_{el}^0$

$$\hat{H}_{el}^0 = \begin{pmatrix} E_{D_0}^{\text{RASCI}} & 0 & \cdots & 0 \\ 0 & E_{D_1}^{\text{RASCI}} & \cdots & 0 \\ \vdots & \vdots & \ddots & \vdots \\ 0 & 0 & \cdots & E_{D_{29}}^{\text{RASCI}} \end{pmatrix}, \tag{35}$$

which was used as zeroth order Hamiltonian for the following pCAP calculations. The smooth Voronoi complex absorbing potential was used with an optimal cutoff radius of 1.9 a_0 was determined by minimizing Eq. (32) of the pCAP trajectories (i.e., the real and imaginary parts of the complex resonance energies as a function of η; see also Lst. A.2 and Fig. A.3 in Appendix A.2). Using this cutoff radius, optimal state-specific values for the CAP strength obtained from the stationary of the corrected pCAP trajectories (Lst. A.3 and Tab. A.7 in Appendix A.2). The resonance positions and widths were extracted from the pCAP trajectories.

4. Results and Discussion

In section 4.1, the results of the Hermitian electronic structure calculations are shown. We begin with a comparison of the ground-state electronic structure of the neutral and radical anion biphenyl triflate species. The radical anion is then analyzed in more detail, with focus on the excited states with TD-DFT. Next, improvements in the excited states description obtained with CASSCF and SC-NEVPT2 are illustrated. Finally, an explicit treatment of the electronic resonance states of the radical anion with pCAP-RASCI is presented in section 4.2.

4.1. Hermitian Electronic Structure Calculations

4.1.1. Ground-state Optimization

The DFT optimized ground-state geometries of the neutral and radical anion biphenyl triflate species are shown in Fig. 4.1 (see Tab. A.1- A.4 in Appendix. A.1.1 for the corresponding molecular coordinates).

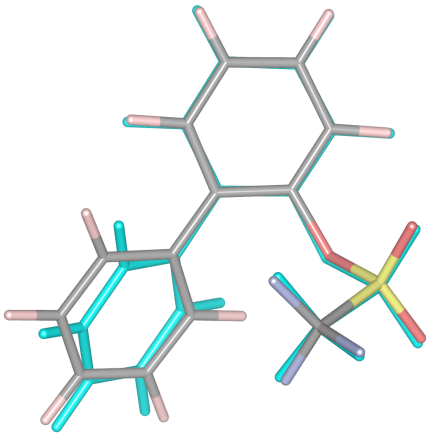

Figure 4.1.: Minimum energy structure of neutral biphenyl triflate (cyan) in the background and its radical anion, with the latter colored by element (C: gray, F: light red, O: dark red and S: yellow).

The root mean squared distance between the neutral and radical anion species of biphenyl triflate is 0.38 Å, indicating a significant structural rearrangement upon reduction. While the upper phenol ring connected to the triflate group and the triflate group align well in both species, substantial differences are observed in the lower phenyl ring as the neutral biphenyl triflate adopts a more twisted geometry than the radical anion. This behavior is consistent with studies on biphenyl which report a reduction in the torsional angle upon reduction due to increased

delocalization of the populated π^* orbital over the aromatic scaffold, consistent with the orbital analysis presented later (see Fig. 4.3).[64]

4.1.2. Comparison of the Stability of Neutral and Biphenyl Triflate Radical Anion

To assess the relative stability of the neutral and radical anion biphenyl triflate species, their ground-state energies were compared in vacuum and in CPCM(DMSO). As shown by Fig. 4.2 a), the relative stability of the two species strongly depends on the environment. While the radical anion is lower in energy than the neutral molecule in CPCM(DMSO), the neutral species is more stable in vacuum. The calculated vertical adiabatic electron affinity in vacuum is +0.20 eV, indicating that the radical anion corresponds to a metastable electronic resonance state rather than a bound anion. While CPCM tries to incorporate solvent effects through a dielectric continuum polarization of the solute charge distribution, it does not describe the coupling of the electronic resonance to the continuum.[9,10,52,53] The resonance character of the state may be artificially suppressed, leading to an overestimation of its stability in solution. Thus, the stabilization of the radical anion predicted in CPCM(DMSO) should be interpreted with caution. As will be further shown in section 4.2, the ground-state represents an electronic resonance state, suggesting that the continuum plays a crucial role and is not captured within the solvation model used.

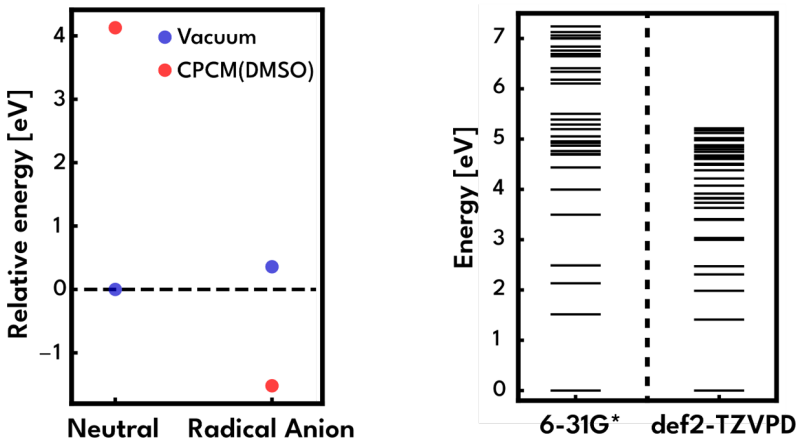

Figure 4.2.: Computed ground- and excited state energies of neutral and radical anion biphenyl triflate species. **a)** Relative ground-state energies of neutral and radical anion species of biphenyl triflate in vacuum and CPCM(DMSO), referenced to the neutral species in vacuum. **b)** Vertical excitation energies of the first 30 excited states of the radical anion calculated with a UKS ωB97X-D3 level of theory with 6-31G* (left) and def2-TZVPD (right).

The radical anion is not a true bound state but embedded into the continuum due to the resonance behavior. However, the continuum is discretized in a finite basis. The extent to which the coupling of the electronic resonance to the continuum is described depends strongly

on the basis set. Finite Gaussian basis sets, in particular those lacking sufficiently diffuse basis functions, do not properly describe continuum-like states. As a result, the coupling between the resonance and the continuum is effectively suppressed, and the resonance may artificially appear as a bound state which can be treated with conventional bound state methods. The inclusion of increasingly diffuse basis functions improves the description of the continuum and enhances this coupling, thereby recovering the metastable character of the state. By increasing the size of the basis set and including more diffuse basis functions, the representation of diffuse continuum-like states is improved continuously, leading to a denser manifold of continuum-like states in which the resonance is embedded.[9] Fig. 4.2 b) shows the vertical excitation energies of the first 30 excited states in the biphenyl triflate radical anion. The density of excited states increases significantly with def2-TZVPD in comparison to the smaller basis set 6-31G*. While the low-lying excited states remain energetically distinguishable, the higher-lying excited states form a dense manifold of states. Thus, bound state calculations may still provide a qualitatively correct description for low-lying excited states (up to sixteenth excited state), whereas higher-lying excited states should be treated with caution.

4.1.3. Ground-State Analysis of Neutral and Biphenyl Triflate Radical Anion

4.1.3.1. Orbital Analysis

The highest occupied molecular orbital (HOMO) of the neutral biphenyl triflate species is a π orbital predominantly localized on the biphenyl fragment, while the lowest unoccupied molecular orbital (LUMO) is the corresponding π^* orbital with additional σ^*(S–O) character as shown in Fig. 4.3.

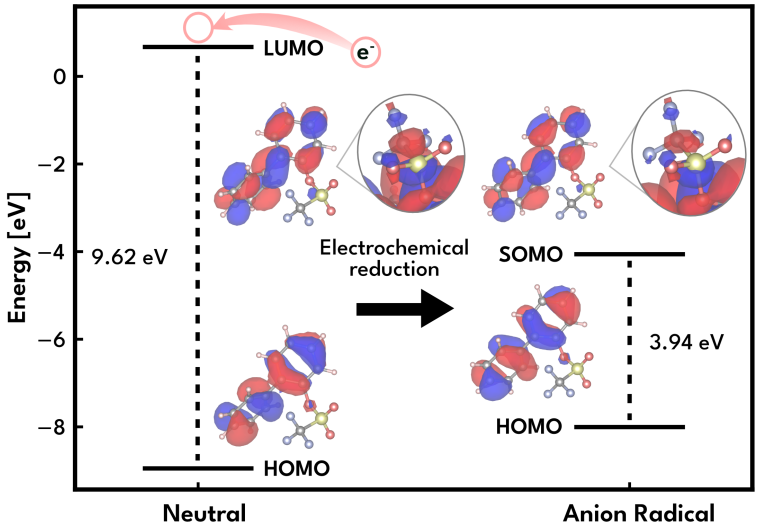

Figure 4.3.: Orbital diagrams of the HOMO and LUMO (neutral), as well as HOMO and singly occupied molecular orbital (SOMO) (radical anion) of biphenyl triflate, visualized at an isovalue of 0.03 a.u. A lower isovalue of 0.01 a.u. was employed for zoomed-in representation highlighting σ^*(S–O) contributions in the LUMO and SOMO. Molecules are colored by element (C: gray, F: light red, O: dark red and S: yellow).

The resulting HOMO-LUMO gap is 9.62 eV. Upon electrochemical reduction, the LUMO becomes singly occupied, forming the biphenyl triflate radical anion. The formed SOMO of the radical anion retains the character of the LUMO from the neutral species. The HOMO-SOMO gap is reduced to 3.94 eV. The enhanced reactivity of the radical anion with respect to the neutral species is primarily attributed to the occupation of antibonding orbitals. The observed slow cleavage of the sulfur-oxygen bond in the absence of light results from the population of an orbital with σ^* character along the S–O bond, as visible in the zoomed-in representation of the SOMO of the radical anion in Fig. 4.3. Our findings show that the S–O bond cleavage becomes accessible in the ground-state upon electrochemical reduction by populating an orbital with σ^*(S–O) contribution, explaining the experimentally observed S–O bond cleavage without light irradiation.

4.1.3.2. Charge and Spin Density Analysis

Following bond cleavage, different products may be formed depending on the localization of charge and spin between the biphenyl scaffold and the leaving group. To assess the thermodynamically favored products and to confirm the anticipated localization of spin and charge (see Fig. 1.2), the reaction energies E_{React} were evaluated according to

$$E_{\mathsf{React}} = (E_{\mathsf{P}_1} + E_{\mathsf{P}_2}) - E_{\mathsf{E}}, \tag{36}$$

where E_{P_1} and E_{P_2} are the absolute energies of the product fragments (biphenyl moiety and leaving group, respectively) and E_{E} is the energy of the biphenyl triflate radical anion. Two electronic configurations need to be considered (see Fig. 4.4).

In the first structural configuration, the unpaired electron is localized on the biphenyl scaffold, while the negative charge resides on the leaving group (Fig. 4.4 a)). This product distribution corresponds to the experimentally proposed reaction products and is chemically intuitive, as the radical is efficiently stabilized within the aromatic biphenyl fragment through delocalization of the spin density over the conjugated π system. The triflate leaving group provides favorable stabilization by delocalization of the negative charge due to the strong electron-withdrawing fluorine atoms.

In the alternative configuration, the product distribution is reversed, resulting in a biphenyl-centered anion and a radical leaving group (Fig. 4.4 b)). Such a distribution is expected to be less thermodynamically favored as the radical is not stabilized electronically and the negative charge is not efficiently delocalized.

For S–O bond cleavage, the thermodynamically preferred scenario corresponds to a biphenyl-centered radical and charge localization on the leaving group, with E_{React} of -39.93 kcal/mol, compared to -11.25 kcal/mol for the alternate distribution. A similar trend is observed for the C–O bond cleavage (-32.17 kcal/mol, compared to 62.06 kcal/mol, respectively). The product distribution consisting of the the biphenyl fragment anion and the triflate radical even exhibits a positive E_{React}. Herein, the radical is no longer stabilized on the biphenyl fragment, leading to thermodynamically highly unfavorable products. These results confirm the experimentally proposed electronic structures of the reaction products following S–O and C–O bond cleavage of the radical anion. The pronounced stabilization can be further rationalized by considering both charge and spin delocalization of the thermodynamically more favored products.

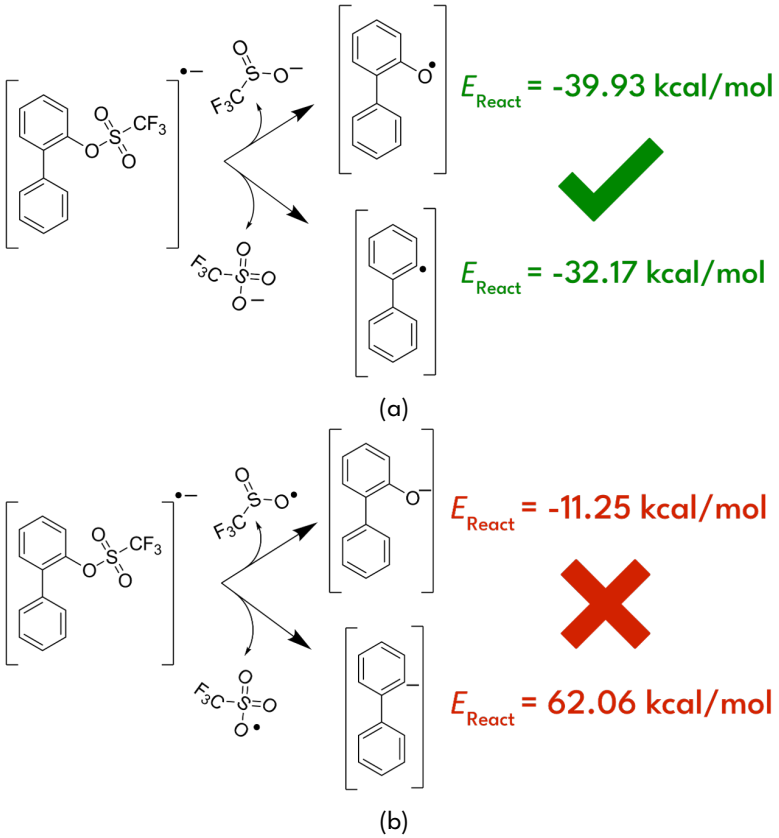

Figure 4.4.: Possible product distributions following S–O and C–O bond cleavage in biphenyl triflate radical anion. **a)** Experimentally proposed product distribution (see Fig. 1.2). The radicals are located in biphenyl fragment, while anion is located in the leaving group. **b)** Alternative product distribution with anion located in biphenylf ragment and radical located in leaving group. Reaction energies (E_{React} of the thermodynamically preferred products are labeled green, while less favorable product distributions are indicated in red.

The Hirshfeld charge population and the spin density were analyzed for the radical anion and the thermodynamically favored products. As shown by the Hirshfeld charge population analysis in Fig. 4.5, the negative charge is located mainly on the triflate group in both bond cleavage cases. The carbon and sulfur atoms within the triflate group are partially positive charged due to the strongly electronegative neighboring fluorine and oxygen atoms, respectively. In contrast, the biphenyl moiety has a less electronegative environment, leading to negligible charge accumulation in the aromatic rings. The negative charge resides primarily on the leaving group for both bond cleavages. The oxygen-centered radical possesses a positively polarized carbon and a negatively charged oxygen atom. The carbon-centered radical, on the contrary, is largely neutral as electronegative groups are absent. The triflyl and triflate anions exhibit nearly equivalent charge distribution over the oxygen atoms, reflecting resonance stabilization.

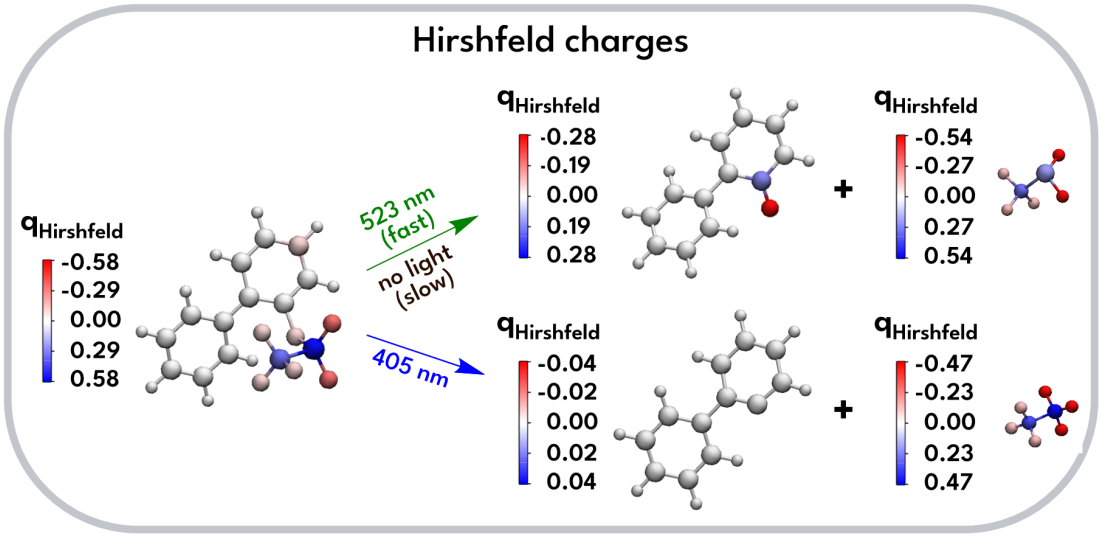

Figure 4.5.: Hirshfeld charges $q_{Hirshfeld}$ for the biphenyl triflate radical anion, oxygen- and carbon-centered radical products, as well as for triflyl and triflate anion side products. The color bars shown to the left of the molecular structures represent the magnitude of the atomic charges, where red indicates negative and blue indicates positive charge accumulation. Ground-state structures were used for the population analysis. Atoms are colored by charge population (negative charge: red and positive charge: blue).

In order to obtain an accurate picture of the localization of the unpaired electrons, the spin density was analyzed for the radical anion and the product radicals. The spin density ρ_S is defined as

$$\rho_S = \rho_\beta - \rho_\alpha, \tag{37}$$

where ρ_β and ρ_α denote the β electron and α electron densities, respectively. The evolution of the ground-state spin densities during the reaction is illustrated in Fig. 4.6. The differences in spin density localization explain the different stability of the dissociation products. The spin density of the radical anion is delocalized over the whole aromatic fragment. The oxygen-centered radical is stabilized by delocalization of spin density over the phenol ring. In contrast, the carbon-centered radical is more localized and therefore less stabilized.

Our findings suggest that substituent effects which further stabilize either of the two product radical species may influence the preferred bond cleavage pathway by changing the relative stability of the products and therefore also the product distribution.

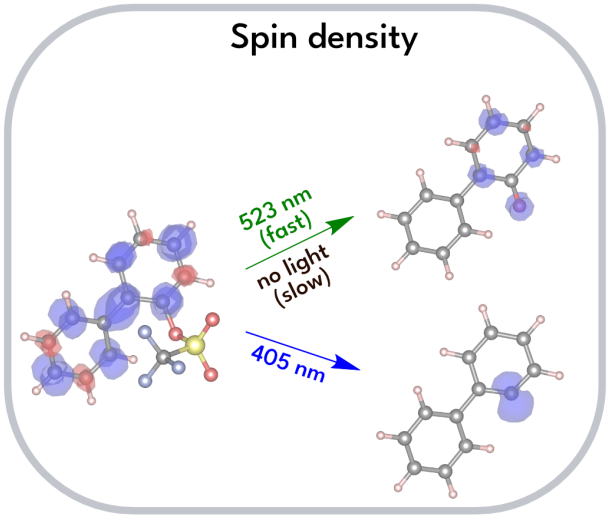

Figure 4.6.: Spin density in biphenyl triflate radical anion, product oxygen- and carbon-centered radicals. Ground-state structures were used for the spin density analysis. An isovalue of 0.0026 a.u. was used for the radical anion, while an isovalue of 0.013 a.u. was used for the oxygen- and carbon-centered radicals. The atoms are colored by element (C: gray, F: light red, O: dark red and S: yellow).

4.1.3.3. Vibrational Analysis

Bond cleavage processes can be described along normal mode coordinates. As S–O bond cleavage also occurs in the ground-state, a matching normal mode was identified in which the sulfur atom and the oxygen atom bound to the biphenyl fragment move away from each other, indicating S–O bond elongation. This normal symmetric stretching mode was calculated with DFT to be at 894 cm^{-1} and exhibits a high intensity, as shown in Fig. 4.7. This aligns with usual reported frequencies of 900-1500 cm^{-1} for S–O motions.[65]

Additionally, the radical anion shows weaker high-frequency bands in the range of 3168-3233 cm^{-1} attributed to multiple coupled C–H stretching vibrations within the biphenyl fragment. Further intense features in the infrared spectrum arise from additional C–H stretching vibrations (coupled vibrational motion in the biphenyl fragment) at 1611 cm^{-1} and 972 cm^{-1}, as well as an asymmetric stretching motion of C_4–F_2 (see atom labeling in Fig. 4.7) at 1197 cm^{-1}. No imaginary vibrational modes were found, indicating that the optimized geometry corresponds to a minimum on the potential energy surface.

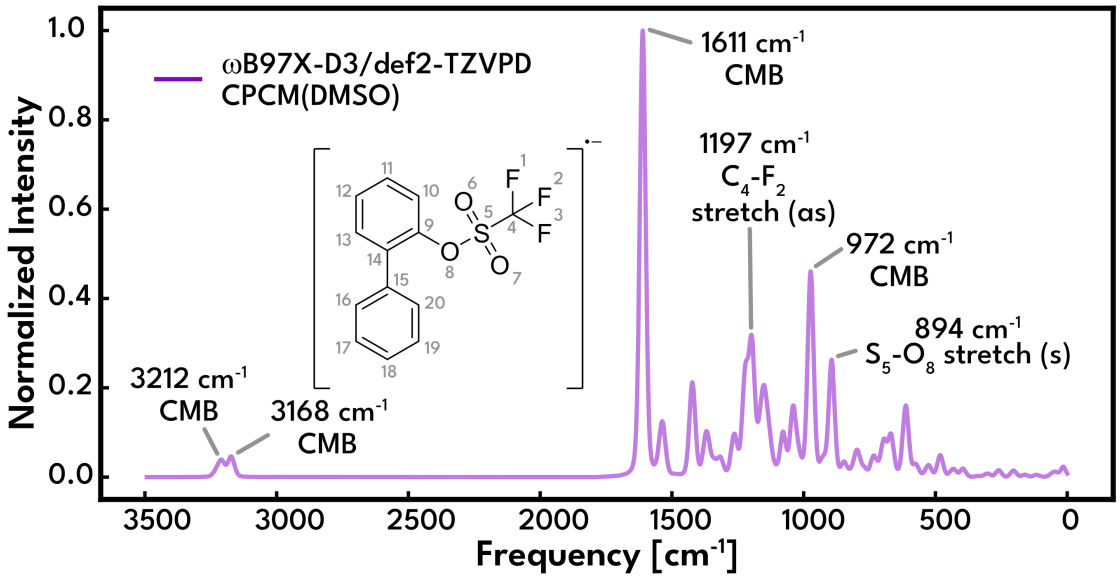

Figure 4.7.: Infrared spectrum of biphenyl triflate radical anion. Atoms are numbered in gray. Peaks with intensities higher than that of the vibrational mode associated with S–O bond cleavage (symmetric stretch S_5–O_8) are labeled. Symmetric and asymmetric stretching modes are denoted by s and a, respectively, while coupled vibrational motions in the biphenyl fragment are abbreviated as CMB. A FWHM of 10 cm^{-1} was used. All vibrational modes are summarized in Tab. A.5 in Appendix A.1.3.

In contrast, no prominent vibrational mode corresponding to a C–O bond cleavage in the ground-state was found. Overall, the calculated vibrational modes of the C–H stretching motions within the biphenyl fragment and the S–O stretching vibration are in good agreement with typical experimental infrared frequencies reported in the literature[65] and support the experimentally observed S–O bond cleavage without light irradiation.

4.1.4. TD-DFT Excited State Calculations

To extend the understanding of the mechanism behind the bond cleavages, the excited states were first investigated by calculating the absorption spectrum with TD-DFT. The results obtained were analyzed with the TheoDORE program package. Fig. 4.8 gives an overview of the calculated excited states including their vertical excitation energies, oscillator strengths and charge-transfer (CT) character. The 30 lowest excited states of the radical anion include 27 doublet and 3 quartet states. The lower panel shows a mostly mixed character of the excited states. In general, the most dominant CTs arise from the phenyl and phenol ring.

The brightest doublet states are D_3 and D_{11}-D_{13}, while the brightest quartet state is Q_3 as illustrated in the energy plot. The excited states representing continuum states are characterized by diffuse particle orbitals and show increased phenyl-to-triflate (orange bar) and phenol-to-triflate (light blue bar) CT. Upon electrochemical reduction of the neutral biphenyl

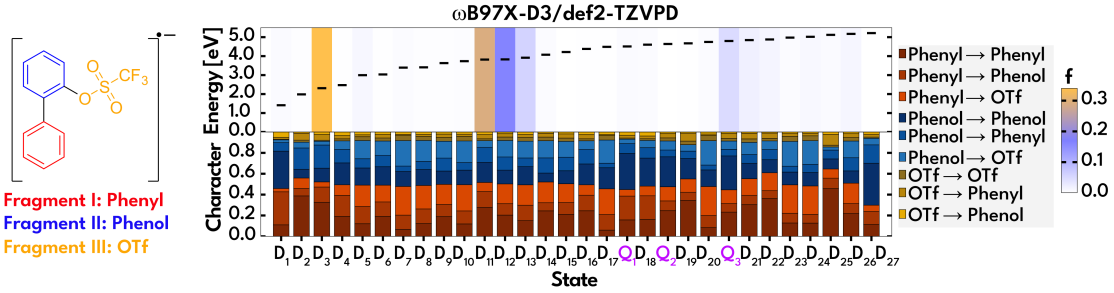

Figure 4.8.: TheoDORE analysis of all computed TD-DFT doublet (black) and quartet (purple) states. The left panel illustrates the fragment splitting of the biphenyl triflate radical anion used in the TheoDORE analysis. CT characters are color-coded as indicated in the legend. Vertical excitation energies of the excited states are shown in the upper panel by horizontal black lines and the bar color represents the oscillator strength f.

triflate species, the additional electron is more weakly bound and delocalized over a larger region within the molecule. This results in an enhanced contribution of long-range CT and diffuse excitations into the triflate fragment where the experimentally observed bond cleavages occur. In general, CTs arising from the triflate group only show minor contribution as the triflate fragment primarily acts as an electron acceptor due to the presence of low-lying σ^* orbitals. The bright doublet states D_3 and D_{11} show similar CT contributions, while mainly differing in their phenol-to-phenol (dark blue bar) excitation and phenol-to-phenyl CT. States D_{12} and D_{13} show CT characters similar to D_{11}, but with an increased phenyl-to-triflate CT contribution.

The three quartet states exhibit similar CT characters, being dominated by phenol-to-phenol, phenyl-to-phenyl (brown bar) and phenyl-to-phenol (burnt orange bar) CT. They show only minor variations in their phenyl-to-phenyl excitations.

Fig. 4.9 compares the TD-DFT and the experimental[8] absorption spectrum of the radical anion in DMSO. The experimental spectrum shows one bright peak at ca. 3.5 eV and a noisy region starting from 4.5 eV, which is attributed to the solvent.[8]. The TD-DFT spectrum shows four peaks representing D_3, D_5, D_{11} and D_{21}. When shifting D_{11} towards lower energies, the bright states D_3 and D_5 are not found in the experimental absorption spectrum. We assume that D_3 and D_5 are not experimentally resolved as own absorption signals but appear in the experiment as the broad absorption band from 3.31 eV to 3.85 eV (322.00 nm to 375.00 nm). The best agreement with the experimental spectrum is therefore obtained when hypsochromically shifting the theoretical spectrum by 1.24 eV. This is a relatively large shift compared to typical reported TD-DFT errors which are usually in the range of 0.2-0.4 eV.[66] Furthermore, TD-DFT typically tends to overestimate the vertical excitation energies, resulting in hypsochromically shifted absorption spectra.[66] The large deviation, together with the unusual direction of the shift may result from the improper description of the coupling to the continuum which might significantly affect the absorption spectrum. In order to describe the coupling to the continuum, complex methods explicitly designed for unbound states such as pCAP are needed.[9] Thus, the TD-DFT results should be interpreted with caution. When shifting the theoretical spectrum towards higher energies, D_{11} overlaps with the noisy experimental region originally assigned as

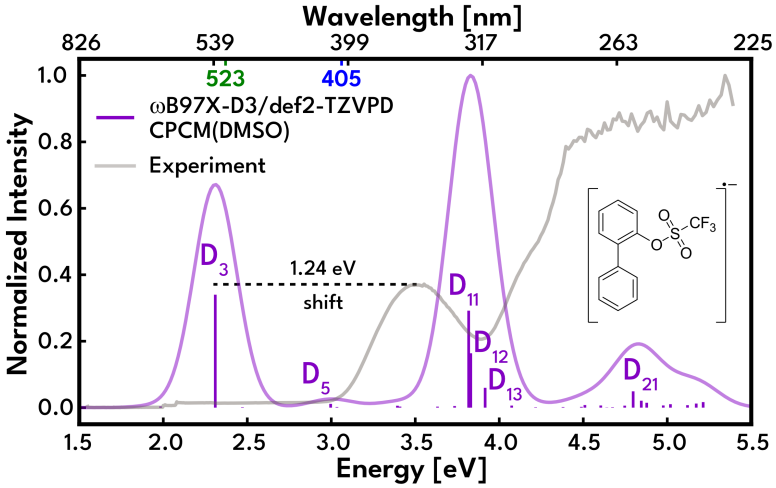

State	Energy [eV]	Oscillator strength f	Main transitions (weight)
$D_{3,\alpha}$	2.31	0.340	$\boldsymbol{\pi_1^*} \rightarrow \pi_4^*$ (0.96)
$D_{5,\alpha}$	3.00	0.0115	$\boldsymbol{\pi_1^*} \rightarrow \sigma^*$(C–O) (0.98)
$D_{11,\alpha}$	3.82	0.291	$\boldsymbol{\pi_1^*} \rightarrow \pi^*$(S–C) (0.36)
$D_{11,\beta}$	3.82	0.291	$\pi_2 \rightarrow \boldsymbol{\pi_1^*}$ (0.55)
$D_{21,\alpha}$	4.80	0.0492	$\boldsymbol{\pi_1^*} \rightarrow \sigma^*$(S–C) (0.34) $\pi_4 \rightarrow \boldsymbol{\pi_2^*}$ (0.16) $\pi_3 \rightarrow \pi_3^*$ (0.11)

Figure 4.9.: Comparison of normalized theoretical ωB97X-D3/def2-TZVPD absorption spectrum (violet) with the experimental spectrum (gray), calculated in DMSO. Excitation wavelengths used for S–O bond cleavage ($\lambda' = 523$ nm, green) and C–O bond cleavage ($\lambda'' = 405$ nm, blue) are indicated. The labeling of the orbitals was adapted from Fig. 3.1. Orbitals with σ^*(S–O) contributions are labeled in bold. Theoretical spectra were broadened using a FWHM of 0.3 eV. Selected excitations are detailed below, showing dominant (weights > 0.10) particle–hole contributions and their weights. The labels α and β denote the spin channel of the main excitation.

solvent artifact.[8] This indicates that the radical anion shows an additional absorption feature at 275 nm overlapping with a solvent artifact. The theoretical spectrum additionally shows several bright higher-lying excited states with D_{21} being the most intense. According to the vertical excitation energies, D_3 is populated by green (λ' = 523 nm) and D_5 by blue light (λ'' = 405 nm). As shown by the natural transitions orbitals in Fig. 4.10, D_3 has $\boldsymbol{\pi_1^*} \rightarrow \boldsymbol{\pi_4^*}$ and D_5 has $\boldsymbol{\pi_1^*} \rightarrow \sigma^*$(C–O) character.

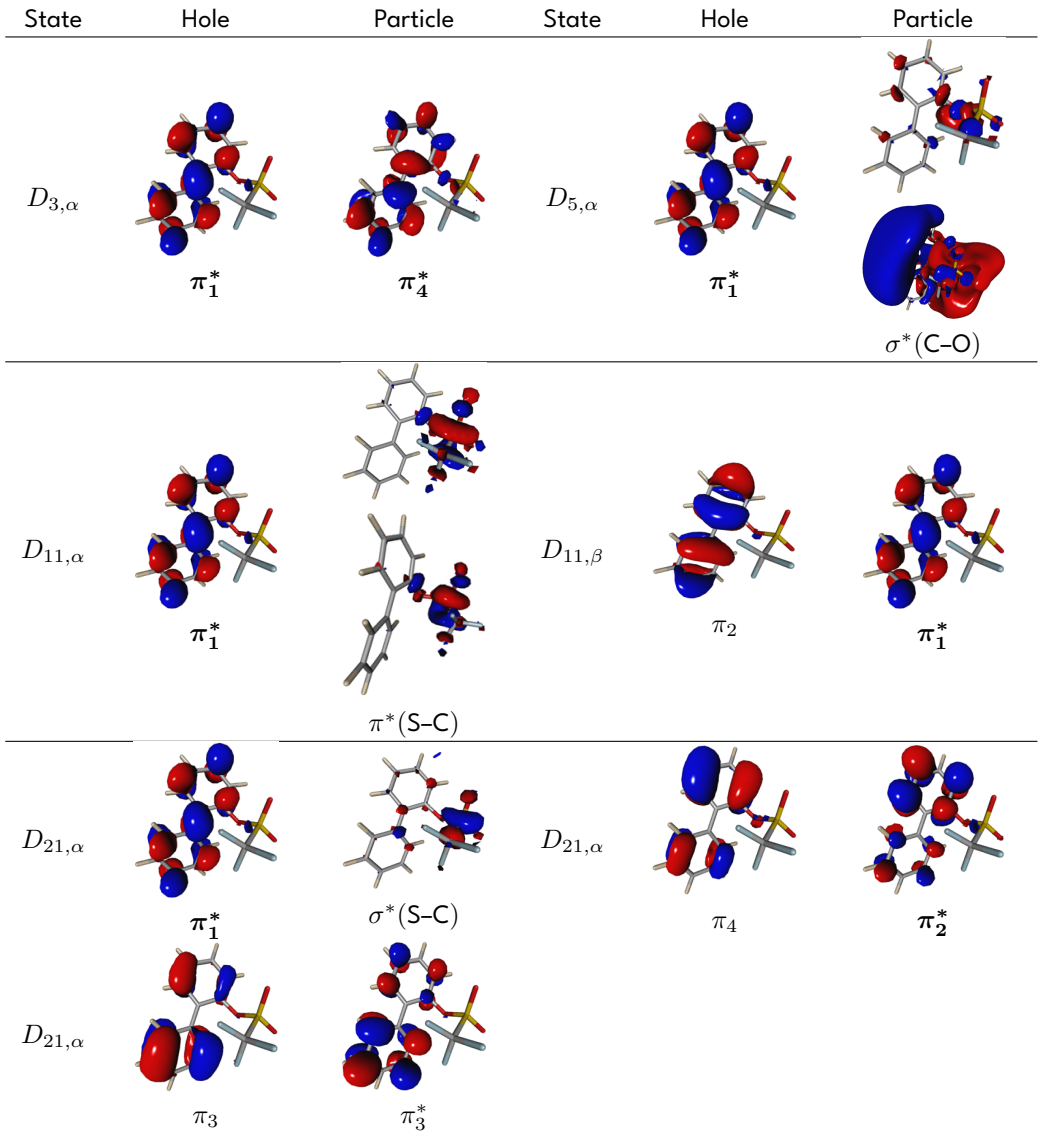

Figure 4.10.: Natural transition orbitals of the selected excited states listed in Fig. 4.9. Hole and particle orbitals are shown for the dominant hole–particle contributions (weights > 0.10). Orbitals with σ^*(S–O) contribution are labeled in bold. An isosurface cutoff value of 0.03 a.u. was used. To better visualize the continuum-like contributions of the σ^*(C–O) orbital, the particle orbital is additionally shown with a reduced isosurface cutoff value of 0.01 a.u., below the corresponding representation at 0.03 a.u. Molecules are colored by element (C: gray, F: light red, O: dark red, S: yellow).

The σ^*(C–O) orbital further exhibits diffuse contributions (see zoomed-in representation of σ^*(C–O) in Fig. 4.10), reminescent of continuum-like states. Thus, D_5 might already be affected by the continuum. Further validation is needed by more sophisticated electronic structure meth-

ods, discussed in the following. The higher-lying excited states D_{11} and D_{21} show antibonding density on the S–C bond of the triflyl anion group. This may be indicative of a third wavelength-selective bond cleavage, as a σ^*(S–C) orbital is populated upon excitation into D_{21}. When considering the theoretical shift of 1.24 eV to the experimental absorption spectrum, experimental screening of the ultraviolet absorption region is needed to confirm the potential third bond cleavage. Studies have revealed such a S–C bond cleavage for phenyl trifluoromethanesulfonate.[67] Instead of electrochemical reduction followed by light irradiation, an electron beam was used to generate the radical anion which undergoes S–C bond cleavage. In the subsequent analysis, this potential third bond cleavage is not considered as it lacks experimental validation. The higher-lying excited states around D_{21} are energetically close to each other as shown by the excited state analysis (Fig. 4.8), resembling continuum-like states. While the obtained TD-DFT results qualitatively reproduce the nature of the excited states, the quantitative description of vertical excitation energies and the coupling effects from the electronic resonance to the continuum should be interpreted with caution within the employed TD-DFT protocol.

4.1.5. Multiconfigurational Excited State Calculations

The active space used to describe the FC point at a CASSCF level of theory consists of the π and π^* scaffold. Fig. 4.11 shows a comprehensive overview of the calculated doublet excited states at a (9, 9) CASSCF/def2-TZVPD CPCM(DMSO) level of theory. The results were analyzed using the TheoDORE program package. The character of the CASSCF states does not add up to one, unlike in TD-DFT as CASSCF wavefunctions are multiconfigurational and can include contributions beyond single-excitation like configurations. The total CT character generally decreases with increasing vertical excitation energies, indicating that higher-lying excited states are less dominated by single-excitation like configurations and exhibit an increasing degree of configurational mixing. While D_1 is primarily characterized by phenol-to-phenol (dark blue bar) excitation and phenyl-to-phenol (burnt orange bar) CT, excited states D_2-D_4 are instead dominated by phenyl-to-phenyl excitation and phenol-to-phenyl (sapphire bar) CT. Additionally, these states show increased CT contributions to the triflate group with respect to D_1, making them more likely to be involved in the excited state bond cleavages. The general trend observed in the TD-DFT CT analysis that CT from the triflate fragment is the least pronounced, is retained at the CASSCF level of theory. The higher-lying excited states (D_5-D_9) exhibit only minor CT contributions to the triflate fragment, while showing predominantly phenyl-to-phenyl, phenol-to-phenol excitation and phenyl-to-phenol CT. Overall, the CT analysis of the CASSCF excited states reveal that D_2-D_4 are most likely candidates for the excited state S–O and C–O bond cleavage. The CASSCF and TD-DFT states show a largely consistent CT character of the excitations for the first four TD-DFT doublet states. In both methods, D_1-D_4 are predominantly described by phenyl-to-phenyl and phenol-to-phenol excitations, along with phenol-to-triflate (light blue bar) CT contributions. Additional contributions from phenyl-to-phenol CT are observed, whereas excitations originating from the triflate fragment itself remain minor.

Differences arise primarily for the higher-lying states. Within TD-DFT, an increased number of states with pronounced phenyl-to-triflate (orange bar) and phenol-to-triflate CT characters are observed due to the presence of continuum states. In contrast, such states are less prominent in CASSCF, where the absence of diffuse orbitals and the multiconfigurational treatment limit

the description of these highly delocalized excitations.

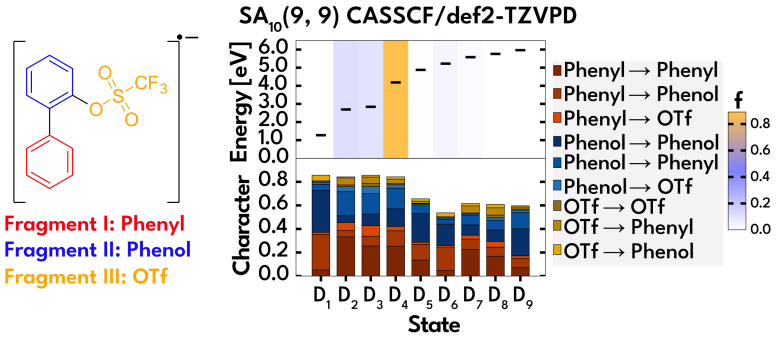

Figure 4.11.: TheoDORE analysis of all computed CASSCF doublet states. The left panel illustrates the fragment splitting of the biphenyl triflate radical anion used in the TheoDORE analysis. CT characters are color-coded as indicated in the legend. Vertical excitation energies of the excited states are shown in the upper panel by horizontal black lines and the bar color represents the oscillator strength f.

To obtain a simplified picture of the potential energy surfaces, a state correlation diagram was constructed including the DFT-optimized FC and the two dissociated structures (Fig. 4.12). In order to suppress the continuum-like contributions and focus on the valence electronic structure relevant for bond cleavage, a moderately small basis set (6-31G*) was used.

For the FC point and the C–O dissociation pathway, a (9, 10) active space was employed, including the π and π^* scaffold, as well as the σ_1^* orbital representing the SOMO in the C–O dissociation limit. In contrast, the S–O dissociation pathway requires a (7, 10) active space. Upon S–O bond cleavage, the SOMO character changes from $\boldsymbol{\pi_1^*}$ at the FC geometry to π_4 at the dissociation limit. Attempts to enforce a common active space led to an unphysical description of the FC electronic structure as the character of the SOMO was artificially reassigned to a different orbital. The resulting state correlation diagram should therefore be interpreted in terms of relative ordering and character of the diabatic states. No solvent was taken into consideration as the radical anion transforms from an unbound state at the FC point to a bound state at the dissociation limits. Thus, a consistent solvent behavior across all three geometries cannot be achieved and no implicit solvent effects were included.

An approximate dissociation energy E_D, can be inferred from the state correlation diagram as the energy difference between the ground-state at the FC geometry and the ground-state at the corresponding dissociation limit. The asymptotic regions of the potential energy surfaces are represented by the dissociated structures. This yields $E_\mathrm{D} = -20.43$ kcal/mol for S–O and $E_\mathrm{D} = -57.97$ kcal/mol for C–O bond cleavage. However, these values for E_D have to be interpreted with caution and are discussed only qualitatively. First, the active space is not strictly consistent across all geometries as the number of active electrons is different at the S–O dissociation limit and the FC point. Thus, the electronic structure is not described at the same level of theory across all geometries. Additionally, the system evolves from a resonance state at the FC geometry to bound electronic states at the dissociation limits. The resulting energy differences therefore do not correspond to well-defined thermodynamic dissociation energies

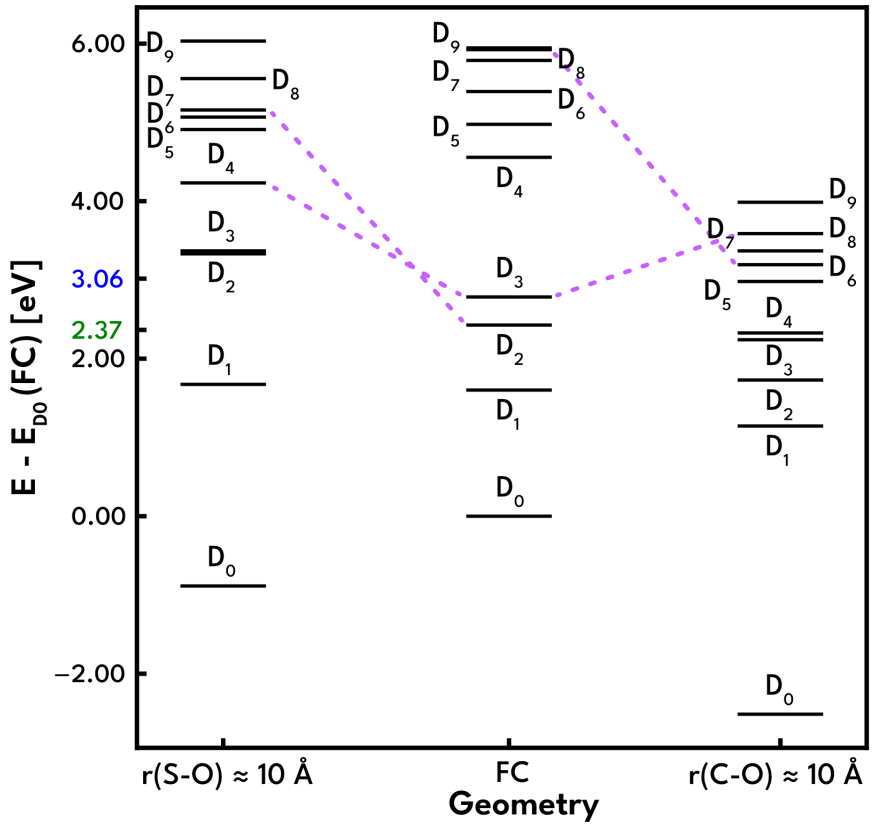

State	r(S–O) ≈ 10Å Orbital transition	Franck–Condon Orbital transition	r(C–O) ≈ 10Å Orbital transition
D_0	π_4	$\boldsymbol{\pi_1^*}$	σ_1^*
D_1	$\pi_2 \rightarrow \pi_4 + \boldsymbol{\pi_1^*}$	$\boldsymbol{\pi_1^*} \rightarrow \boldsymbol{\pi_2^*}$	$\pi_4 \rightarrow \sigma_1^*$
D_2	$\pi_1 + \pi_2 \rightarrow \pi_4 + \boldsymbol{\pi_1^*}$	$\boldsymbol{\pi_1^*} + \pi_2 \rightarrow \pi_3^*$	$\pi_2 + \pi_3 \rightarrow \boldsymbol{\pi_1^*} + \pi_3^* + \boldsymbol{\pi_2^*}$
D_3	$\pi_3 \rightarrow \pi_4 + \boldsymbol{\pi_1^*}$	$\boldsymbol{\pi_1^*} + \pi_2 \rightarrow \pi_4^*$	$\pi_2 + \pi_4 \rightarrow \sigma_1^* + \pi_3^* + \boldsymbol{\pi_1^*}$
D_4	$\pi_2 \rightarrow \boldsymbol{\pi_1^*} + \pi_4^*$	$\pi_2 \rightarrow \boldsymbol{\pi_1^*} + \pi_4^* + \boldsymbol{\pi_2^*}$	$\pi_3 + \pi_2 \rightarrow \pi_3^* + \sigma_1^* + \boldsymbol{\pi_1^*}$
D_5	$\pi_4 + \pi_1 + \pi_3 + \pi_2 \rightarrow \boldsymbol{\pi_2^*} + \pi_3^*$	$\pi_4 + \pi_2 \rightarrow \boldsymbol{\pi_2^*} + \boldsymbol{\pi_5^*}$	$\pi_2 + \pi_4 + \pi_3 \rightarrow \boldsymbol{\pi_2^*} + \boldsymbol{\pi_1^*} + \pi_3^*$
D_6	$\pi_4 + \pi_3 \rightarrow \boldsymbol{\pi_2^*} + \pi_3^*$	$\pi_2 + \pi_4 \rightarrow \boldsymbol{\pi_2^*} + \pi_4^* + \pi_3^*$	$\pi_3 + \pi_2 \rightarrow \pi_3^* + \boldsymbol{\pi_1^*}$
D_7	$\pi_2 + \pi_4 \rightarrow \pi_3^*$	$\pi_2 + \pi_4 \rightarrow \pi_3^* + \boldsymbol{\pi_2^*} + \pi_4^* + \boldsymbol{\pi_1^*}$	$\pi_2 + \pi_3 \rightarrow \boldsymbol{\pi_1^*} + \pi_3^* + \pi_4^* + \boldsymbol{\pi_2^*}$
D_8	$\pi_3 + \pi_2 \rightarrow \pi_3^* + \boldsymbol{\pi_1^*} + \boldsymbol{\pi_2^*}$	$\pi_3 + \pi_2 \rightarrow \pi_3^* + \boldsymbol{\pi_2^*} + \boldsymbol{\pi_1^*}$	$\pi_3 + \pi_2 \rightarrow \boldsymbol{\pi_1^*} + \pi_3^*$
D_9	$\pi_3 + \pi_2 \rightarrow \boldsymbol{\pi_1^*} + \pi_3^*$	$\pi_3 + \pi_2 \rightarrow \boldsymbol{\pi_2^*} + \pi_3^* + \pi_4^* + \boldsymbol{\pi_1^*}$	$\pi_2 \rightarrow \boldsymbol{\pi_2^*} + \boldsymbol{\pi_1^*}$

Figure 4.12.: State correlation diagram of bond cleavage pathways calculated with (9,10) CASSCF/6-31G* for FC point and C–O pathway, as well as (7,10) CASSCF/6-31G* for S–O pathway. All energies are referenced to the ground-state of the FC point. Excitation energies used for S–O bond cleavage ($h\nu' = 2.37$ eV, green) and C–O bond cleavage ($h\nu'' = 3.06$ eV, blue) are indicated. Dashed purple lines indicate correspondence between the electronic states at the FC geometry and the dissociated structures. Details on the character of the electronic states represented by orbital transitions are shown below, where π^* orbitals with σ^*(S–O) contribution are labeled in bold. The molecular coordinates of the dissociated structures are listed in Tab. A.6 in Appendix A.1.5.

and are not directly comparable to experimental dissociation energies. As no experimental values for E_D are available for the bond cleavage pathways, a quantitative comparison with the experiment is not possible.

Nevertheless, the state correlation diagram is consistent with the experimentally observed wavelength dependence of the two bond cleavage pathways. The lower-lying excited state D_2, exhibiting pronounced σ^*(S–O) character in the FC region, correlates with S–O bond cleavage and is consistent with the experimentally observed bond dissociation under lower-energy irradiation (λ' = 523 nm). In contrast, the C–O bond cleavage is associated with the higher-lying D_3 state and is therefore consistent with the requirement for higher-energy excitation (λ'' = 405 nm). Additionally, the state correlation diagram reveals several crossings between excited states along both dissociation coordinates, indicating the excited state bond cleavage processes. However, most states originating from the FC geometry could not be continuously followed to the dissociation limits, suggesting substantial electronic reorganization and strong state mixing along the reaction coordinates.

Having established a qualitative relationship between the electronic states along the reaction coordinate, the excited states were further analyzed by comparing the absorption spectra at CASSCF/def2-TZVPD and SC-NEVPT2/def2-TZVPD level of theory (Fig. 4.13). According

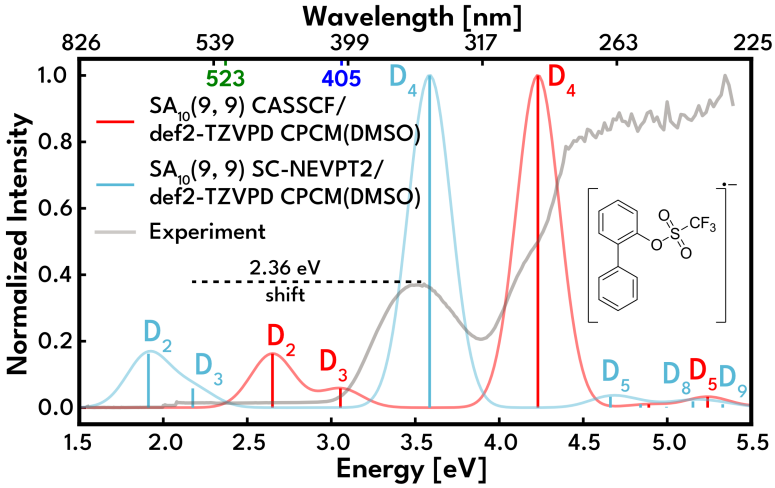

State	E(CASSCF) [eV]	E(SC-NEVPT2) [eV]	Oscillator strength f	Main transitions (weight)
D_2	2.65	1.91	0.146	$\boldsymbol{\pi_1^*} \rightarrow \pi_4^*$ (0.63)
D_3	3.05	2.18	0.0520	$\boldsymbol{\pi_1^*} \rightarrow \pi_3^*$ (0.67)
D_4	4.23	3.59	0.898	$\pi_2 \rightarrow \boldsymbol{\pi_1^*}$ (0.60) $\boldsymbol{\pi_1^*} \rightarrow \pi_4^*$ (0.11)

Figure 4.13.: Comparison of normalized SA_{10} (9, 9) CASSCF/def2-TZVPD (red) and SA_{10} (9, 9) SC-NEVPT2/def2-TZVPD (cyan) spectra with experiment (gray). Excitation wavelengths used for S–O (λ' = 523 nm, green) and C–O bond breakage (λ'' = 405 nm, blue) are indicated. Theoretical spectra were broadened using a FWHM of 0.3 eV. Selected excitations are shown below with dominant orbital transitions (weight > 0.10). Orbitals with σ^*(S–O) contribution are labeled in bold.

to the CASSCF vertical excitation energies, D_2 and D_3 are associated with the experimental absorption band, while D_4 likely interferes with the solvent. Thus, D_2 ($\boldsymbol{\pi_1^*} \rightarrow \pi_4^*$ character) is associated with the S–O bond cleavage and D_3 ($\boldsymbol{\pi_1^*} \rightarrow \pi_3^*$ and $\pi_2 \rightarrow \boldsymbol{\pi_1^*}$ character) for the C–O bond cleavage. This assignment is further supported by the difference in the experimental excitation energies (0.69 eV). At the CASSCF level of theory, the energy gap between D_2 and D_3 amounts to 0.70 eV, while the energy gap between D_3 and D_4 is 1.29 eV. Thus, the close agreement between the experimental and calculated energy separations further supports the assumption that D_2 and D_3 resemble a single experimental absorption band. When comparing SC-NEVPT2 with CASSCF, the SC-NEVPT2 spectrum shows a bathochromic shift, where D_4 shows good agreement with the experimental absorption feature at 350 nm, indicating that D_4 is responsible for the C–O bond cleavage and D_3 for the S–O bond cleavage. Assigning D_4 to the experimental absorption band would imply that the lower-lying bright states D_2 and D_3 show additional absorption bands in the experimental absorption spectrum, which is not observed. However, the magnitude of the deviation of SC-NEVPT2 to the experiment was found to be very large. In particular, the deviation between the vertical excitation energy of D_3 and the experimental absorption maximum amounts to 2.36 eV. This large deviation suggests that the SC-NEVPT2 correction is not physically reliable for the radical anion as it shifts the spectrum even further away from the experiment. SC-NEVPT2 may become unreliable for electronic resonances as the coupling of the reference state to the continuum is not properly described, the energy denominators in Eq. (10) do not behave physically, leading to unreliable perturbation corrections.

Fig. 4.14 shows a comparison of the vertical excitation energies obtained with TD-DFT, CASSCF and SC-NEVPT2. In contrast to TD-DFT, both CASSCF and SC-NEVPT2 show a less dense manifold of excited states as only excitations within the selected (9, 9) active space are described.

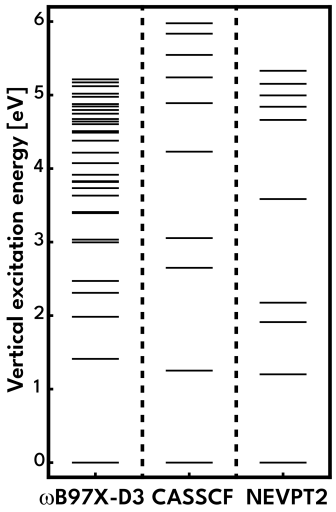

Figure 4.14.: Comparison vertical excitation energies of excited states using TD-DFT, CASSCF and SC-NEVPT2 level of theory with the def2-TZVPD basis set and CPCM(DMSO).

In TD-DFT, more states that are energetically close to each other appear as excitations into diffuse continuum-like states are allowed, while these orbitals are not included in the active space. SC-NEVPT2 in comparison to CASSCF shows regions with a larger density of states with reduced energy gaps between each other. The dynamic correlation added within the SC-NEVPT2 framework stabilizes the excited states and results in a redistribution of the excitation energies.

Although a larger number of excited states (30 states) was calculated with TD-DFT, the corresponding excitation energies remain lower than those obtained from CASSCF and SC-NEVPT2. While 30 TD-DFT roots span an energy range up to approximately 5.2 eV, only 10 roots already extend to about 6.0 eV and 5.3 eV at the CASSCF and SC-NEVPT2 levels of theory, respectively. This indicates that the continuum is suppressed in CASSCF and SC-NEVPT2 due to the restricted active space. To assess whether the size of the basis set affect the character of the excited states, the excited state characters obtained with def2-TZVPD and 6-31G* are compared at a CASSCF level of theory. In the following, we focus on the D_2-D_4.

Notably, a reordering of the excited states was observed when comparing the (9, 9) CASSCF/def2-TZVPD results to a (9, 10) CASSCF/6-31G* level of theory. The second and third excited state switched their character. The fourth excited state exhibits a similar character with both basis sets and predominantly has $\boldsymbol{\pi_1^*} \rightarrow \pi_4^*$ character. This behavior is likely related to the different treatment of diffuse continuum-like states present in the radical anion. The smaller 6-31G* basis set does not provide a description of such states, leading to a more localized and predominantly valence character of the excited states. In contrast, the larger def2-TZVPD basis set introduces diffuse functions that partially describe continuum-like excitations. However, this incomplete representation can lead to artificial mixing between valence and diffuse states, which may alter the qualitative ordering of the excited states. To obtain a consistent description of such diffuse states, a more rigorous computational protocol including the extended diffuse def2-TZVPD+1s1p1d basis set in combination with the pCAP-RASCI method is used in the following.

4.2. pCAP-RASCI

In order to properly describe the unbound states present in the radical anion, the pCAP method is employed. Additional 1s1p1d diffuse basis functions were added on a ghost atom located at the center of mass. The 20 lowest-energy diffuse orbitals were included in the RAS 3 space and 30 states were calculated using the pCAP-RASCI approach.

Electronic resonance states are expected to stabilize at weak pCAP strengths because only a small perturbation is required to absorb the outgoing electron density, whereas diffuse continuum-like states are assumed to require significantly larger η values. Thus, by comparing the η values of the η trajectories (see also Tab. A.7 in Appendix A.2), the four electronic resonance states were identified, namely D_0, D_{20}, D_{21}, and D_{22} (for $\eta < 0.01$). The resonance ground-state D_0 is dominated by $\boldsymbol{\pi_1^*}$ character, while D_{20} corresponds to an excitation from an orbital with $\boldsymbol{\pi_1^*}$ character into a diffuse orbital. The resonance state D_{21} has $\boldsymbol{\pi_1^*} \rightarrow \pi_3^*$ and $\pi_2 \rightarrow \boldsymbol{\pi_1^*}$ character, while D_{22} exhibits predominantly $\boldsymbol{\pi_1^*} \rightarrow \pi_4^*$ character. The CASSCF and SC-NEVPT2 states relevant for bond cleavage (D_0 and D_2-D_4) were identified within the pCAP-RASCI results by comparing their dominant electronic transitions (through orbital transition characters) with the RASCI respective states. As the pCAP correction leads to an energetic reordering of

the RASCI states, a consistent assignment of the relevant states among CASSCF/SC-NEVPT2 and pCAP-RASCI was achieved. In particular, D_0, D_2, D_3 and D_4 at a CASSCF/def2-TZVPD and SC-NEVPT2/def2-TZVPD level of theory correspond to D_0, D_{22}, D_{21} and D_{26} at a pCAP-RASCI/def2-TZVPD+1s1p1d level of theory, respectively.

The autodetachment lifetime τ of the excited states which may be involved in the bond cleavage and the ground-state was obtained from the imaginary part (resonance width Γ) of the complex energy of pCAP-RASCI by

$$\tau = \frac{1}{2|\Gamma|}, \tag{38}$$

where Γ is obtained from the imaginary part of the resonance energy (Eq. 25). The resulting lifetimes are summarized in Tab. 4.1 for the four selected states.

Table 4.1.: Autodetachment lifetimes of selected pCAP-RASCI states relevant for experiment.

pCAP-RASCI State	Γ [a.u.]	τ [fs]
D_0	-0.000146	83
D_{21}	-0.000409	30
D_{22}	-0.001302	9
D_{26}	0.000214	57

The autodetachment lifetime of the ground-state resonance D_0 is 83 fs, indicating that the radical anion is metastable but sufficiently long-lived to undergo bond cleavage. In contrast, the excited resonance states are considerably shorter-lived, with lifetimes of 30 fs for D_{21}, 9 fs for D_{22} and 57 fs for D_{26}. These short lifetimes indicate rapid autodetachment and suggest that these states are unlikely to undergo internal conversion.

Fig. 4.15 shows a comparison between the experimental and the CASSCF, SC-NEVPT2 and pCAP-RASCI absorption spectra (see also Tab. A.7 in Appendix A.2). For simplicity, only the excited states which may be involved in the excited state S–O and C–O bond cleavage are shown.

As oscillator strengths are not directly accessible in pCAP, those of the corresponding CASSCF states were used for the pCAP-RASCI states. This approximation is justified as CASSCF provides well-defined, discrete excited states, while the electronic character of the excited states is fragmented over multiple states in RASCI due to the inclusion of continuum-like states. The widths of the Lorentzians of the pCAP-RASCI states was determined by the imaginary part of the complex resonance energies. When explicitly accounting for the resonance states, the absorption spectrum shows a hypsochromic shift in contrast to the bathochromic shift obtained with SC-NEVPT2. This supports our assumption that the perturbative treatment in SC-NEVPT2 is not physically meaningful for the biphenyl triflate radical anion.

The pCAP-RASCI/def2-TZVPD+1s1p1d results show a reordering of the excited states compared to the CASSCF/def2-TZVPD and TD-DFT/def2-TZVPD level of theory. Notably, the ordering obtained from pCAP-RASCI/def2-TZVPD+1s1p1d is more consistent with the CASSCF/6-31G* results. This behavior suggests that both, neglecting the continuum (as in

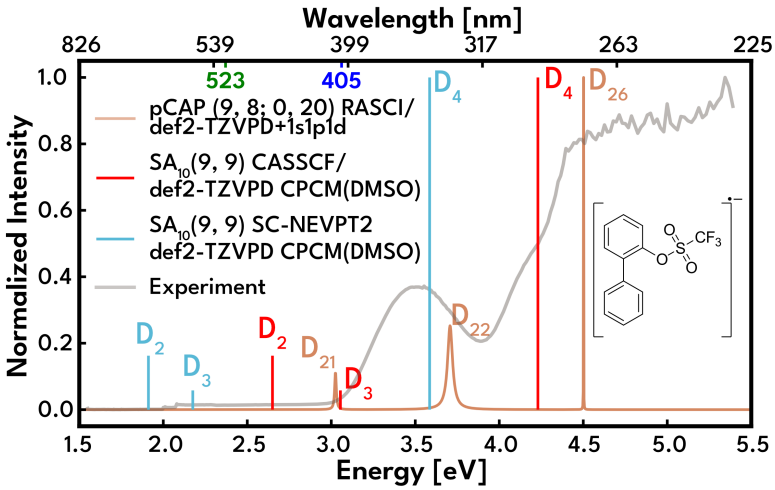

Figure 4.15.: Comparison normalized SA_{10} (9, 9) CASSCF/def2-TZVPD (red), SA_{10} (9, 9) SC-NEVPT2/def2-TZVPD (cyan), pCAP-(9, 8; 0, 20) RASCI/def2-TZVPD+1s1p1d spectra with experiment (gray). The (9, 8; 0, 20) notation denotes 9 active electrons in 8 RAS 2 orbitals, an empty RAS 1 space and 20 orbitals in the RAS 3 space. The Lorentzian broadening of the pCAP-RASCI states was obtained from the imaginary parts of the resonance energies (see Eq. 25).

CASSCF/6-31G*) and treating the continuum consistently (as in pCAP-RASCI), yield a qualitatively similar description, whereas a partial description of diffuse and continuum-like states (as in CASSCF/def2-TZVPD and TD-DFT/def2-TZVPD) can lead to artificial mixing of valence and continuum character and thus to a different, incorrect state ordering. Thus, neglecting the continuum using the moderately small basis set 6-31G*, leads to a qualitatively correct description of valence states, while a partial description of the continuum results in wrong state orderings.

The pCAP-RASCI state D_{21} is responsible for the S–O bond cleavage (CASSCF/SC-NEVPT2 state: D_3), while pCAP-RASCI state D_{22} is responsible for the C–O bond cleavage (CASSCF/SC-NEVPT2 state: D_2). The pCAP-RASCI spectrum further shows a bright peak in the noisy region in the experimental spectrum, representing a second absorption feature of the biphenyl triflate radical anion as further predicted by CASSCF and TD-DFT. The reordering of the states is attributed due to the consistent treatment of the continuum-like states with pCAP-RASCI, similar to neglecting the continuum by using a sufficiently small basis set. These findings highlight that an explicit treatment of the continuum is crucial for a reliable description of the resonance. Based on this, we demonstrated that pCAP-RASCI provides an efficient and consistent description of electronic resonance states in larger molecules.

Attempts to perform relaxed pCAP-assisted potential energy surface scans at the (9, 9) CASSCF/def2-TZVPD level of theory were not successful. We attribute this to mixing of diffuse orbitals during the optimization, preventing a stable description of the active space. In addition to the complex electronic structure of the radical anion and the need to describe two dissociation pathways, maintaining a consistent description of the active space along dissociation proved to be challenging. Additional orbitals and orbital-overlap-tracking are needed to satisfy both dissociation pathways.

5. Conclusions

We investigated the experimentally observed wavelength-selective bond cleavage in the biphenyl triflate radical anion. Electrochemical reduction generates a radical anion which undergoes selective S–O bond cleavage upon excitation at 523 nm and C–O bond cleavage at 405 nm (as shown in Fig. 5.1), while thermal dissociation of the S–O bond dissociation is further observed experimentally. Understanding this wavelength-selective chemistry and the underlying electronic structure of the radical anion is challenging since the radical anion does not correspond to a bound state.

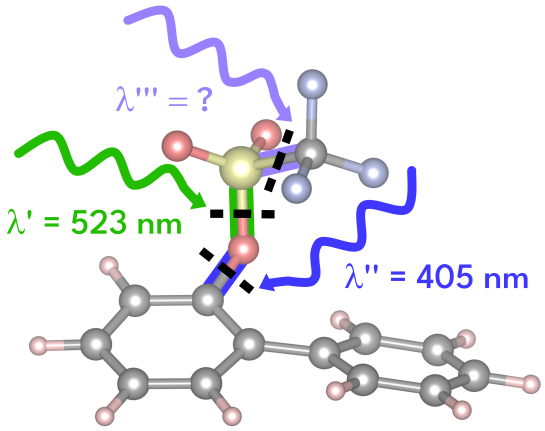

Figure 5.1.: Schematic representation of the experimentally observed S–O bond (λ' = 523 nm) and C–O bond cleavage (λ'' = 405 nm) together with the identified potential third bond cleavage in the excited states. Molecules are colored by element (C: gray, F: light red, O: dark red and S: yellow).

The calculated vertical adiabatic electron affinity in vacuum shows that the radical anion is not a true bound anion but a metastable electronic resonance state. Analysis of the singly occupied molecular orbital revealed occupation of an orbital with σ^*(S–O) contributions, explaining the S–O bond cleavage observed without light irradiation. These findings are further supported by the vibrational analysis, in which a dissociative S–O stretching vibrational mode was found in the ground-state, whereas no analogous mode was identified for the C–O bond cleavage.

The excited state calculations showed that the electronic structure description is highly sensitive to both the level of theory and the basis set. Time-dependent density functional theory (TD-DFT) and complete active space self-consistent field (CASSCF) method yielded qualitatively similar energetic ordering and state assignments for the excited states. It was possible with TD-DFT to identify high-lying excited states with significant σ^*(S–C) contributions, sug-

gesting a potential third bond cleavage pathway under higher-energy irradiation (see Fig. 5.1). To improve the CASSCF spectrum, dynamic correlation was included with strongly correlated n-electron valence state wave function second-order perturbation theory (SC-NEVPT2). However, SC-NEVPT2 led to a large deviation in respect to the experiment, suggesting that the perturbative treatment becomes unreliable for the metastable resonance character of the radical anion.To explicitly account for continuum effects, projected complex absorbing potential (pCAP) restricted active space configuration interaction (RASCI) calculations were performed. Inclusion of the continuum enabled a physically more consistent description of the electronic resonance character and revealed that different excited states are associated with the experimentally observed S–O and C–O bond cleavage pathways than with CASSCF with a diffuse triple-ζ basis set. However, CASSCF calculations employing a compact double-ζ basis set without diffuse functions showed qualitative agreement with the pCAP-RASCI results regarding the ordering of the dissociative valence states. Furthermore, the from pCAP-RASCI extracted ground-state autodetachment lifetime of 83 fs suggests that the resonance state is sufficiently long-lived to undergo bond dissociation. In contrast, the significantly shorter lifetimes of the excited states indicate strong competition between the bond cleavage with the autodetachment of an electron.

The state correlation diagram further revealed excited state dissociation pathways which are connected through state crossings along the dissociation coordinates. Most states at the Franck-Condon point were not identified in the dissociation limits, indicating a significant reordering of the electronic structure in both dissociation pathways. Attempts to compute relaxed excited state potential energy surfaces including pCAP were not successful, likely due to strong coupling between valence and diffuse continuum-like states during the geometry optimization.

Overall, this work demonstrates that electronic resonance states play a central role in the wavelength-selective bond cleavage of the biphenyl triflate radical anion. While traditional electronic structure methods designed for bound states can reproduce qualitative energetic trends, explicit treatment of the electronic continuum is needed to obtain a physically meaningful description of the resonance states and their dissociation pathways. To our knowledge, this represents the largest molecular system explicitly investigated with pCAP. Future nonadiabatic dynamics simulations are needed to obtain a detailed picture of the excited state mechanism and the competition between bond dissociation and electron autodetachment.

A. Appendix

This chapter contains further insights gained during this work.

A.1. Hermitian Electronic Structure Calculations

A.1.1. Geometry Optimization

Python code Lst. A.1 was used to obtain with the MMFF94 force-field optimized structures which were used as reasonable starting guess geometries for the following geometry optimizations.

Listing A.1: Generation of input geometry for subsequent geometry optimization. The code was adapted from Johannes C. B. Dietschreit.

```python
from rdkit import Chem
from rdkit.Chem import AllChem
from typing import Optional


def smiles_to_xyz(smiles: str, filename: str = "coordinates.xyz") -> Optional[Chem.Mol]:

    mol = Chem.MolFromSmiles(smiles)
    if mol is None:
        print("ERROR: Failed to parse SMILES.")
        return None

    mol = Chem.AddHs(mol)

    status = AllChem.EmbedMolecule(mol, randomSeed=0xf00d)
    if status != 0:
        print("ERROR: Embedding (3D coordinate generation) failed.")
        return None

    AllChem.MMFFOptimizeMolecule(mol)

    conf = mol.GetConformer()
    positions = conf.GetPositions()
    atoms = mol.GetAtoms()

    with open(filename, "w") as f:
        f.write(f"{mol.GetNumAtoms()}\n")
        f.write(smiles)
        for atom, pos in zip(atoms, positions):
```

```
30              f.write(f"\n{atom.GetSymbol():2s} {pos[0]:10.5f} {pos
    [1]:10.5f} {pos[2]:10.5f}")
31
32      return mol
```

Tab. A.1- A.4 show a comparison of the MMFF94 force field and DFT optimized structures of the neutral molecule in vacuum and DMSO and the radical anion in vacuum and DMSO, respectively.

Table A.1.: Comparison of the initial (X, Y, Z) and with ωB97X-D3/def2-TZVPD CPCM(DMSO) optimized geometry (X_{opt}, Y_{opt}, Z_{opt}) in Å of neutral biphenyl triflate.

Atom	X [Å]	Y [Å]	Z [Å]	X_{opt} [Å]	Y_{opt} [Å]	Z_{opt} [Å]
O	1.98372	-2.49268	-2.44982	1.9076	-2.3731	-2.4871
S	2.13664	-1.37823	-1.52437	2.0837	-1.3436	-1.5293
O	3.31429	-0.53006	-1.64110	3.2769	-0.5787	-1.4536
O	0.77814	-0.46706	-1.65888	0.8130	-0.4406	-1.6344
C	0.72114	0.80382	-1.13832	0.7312	0.8740	-1.1107
C	1.51558	1.81722	-1.68408	1.5161	1.8637	-1.6687
C	1.44114	3.11304	-1.17762	1.4146	3.1532	-1.1724
C	0.55718	3.40369	-0.14342	0.5291	3.4271	-0.1407
C	-0.26367	2.40007	0.37617	-0.2658	2.4191	0.3799
C	-0.20910	1.08401	-0.11810	-0.1925	1.1113	-0.0991
C	-1.11415	0.06025	0.43289	-1.0832	0.0594	0.4544
C	-2.02234	-0.62409	-0.39152	-1.8879	-0.7134	-0.3803
C	-2.87573	-1.59829	0.13215	-2.7381	-1.6699	0.1523
C	-2.83774	-1.90100	1.49079	-2.7923	-1.8688	1.5253
C	-1.94978	-1.22892	2.32670	-1.9963	-1.1009	2.3634
C	-1.09694	-0.25473	1.80207	-1.1488	-0.1408	1.8313
C	1.93595	-1.96876	0.20088	1.8695	-2.1267	0.1343
F	1.96388	-0.95751	1.11652	1.9080	-1.1980	1.0772
F	0.76806	-2.64471	0.39260	0.7228	-2.7788	0.1961
F	2.93463	-2.82932	0.56234	2.8696	-2.9766	0.3145
H	2.19588	1.61109	-2.50733	2.1960	1.6261	-2.4754
H	2.06869	3.89663	-1.59540	2.0254	3.9394	-1.5977
H	0.49352	4.41525	0.25041	0.4448	4.4330	0.2514
H	-0.96863	2.65721	1.16544	-0.9778	2.6428	1.1654
H	-2.07647	-0.39598	-1.45466	-1.8553	-0.5592	-1.4523
H	-3.57117	-2.11841	-0.52174	-3.3614	-2.2620	-0.5073
H	-3.50094	-2.65981	1.89809	-3.4556	-2.6185	1.9400
H	-1.91799	-1.46404	3.38749	-2.0322	-1.2507	3.4360
H	-0.40380	0.25132	2.47184	-0.5211	0.4512	2.4875

Table A.2.: Comparison of the initial (X, Y, Z) and with ωB97X-D3/def2-TZVPD optimized geometry (in vacuum) (X_{opt}, Y_{opt}, Z_{opt}) in Å of neutral biphenyl triflate.

Atom	X [Å]	Y [Å]	Z [Å]	X_{opt} [Å]	Y_{opt} [Å]	Z_{opt} [Å]
O	1.98372	-2.49268	-2.44982	1.8716	-2.3838	-2.4955
S	2.13664	-1.37823	-1.52437	2.0759	-1.3517	-1.5524
O	3.31429	-0.53006	-1.64110	3.2619	-0.5772	-1.4987
O	0.77814	-0.46706	-1.65888	0.7981	-0.4374	-1.6358
C	0.72114	0.80382	-1.13832	0.7301	0.8678	-1.1084
C	1.51558	1.81722	-1.68408	1.5316	1.8566	-1.6455
C	1.44114	3.11304	-1.17762	1.4306	3.1448	-1.1489
C	0.55718	3.40369	-0.14342	0.5275	3.4248	-0.1359
C	-0.26367	2.40007	0.37617	-0.2793	2.4205	0.3702
C	-0.20910	1.08401	-0.11810	-0.2029	1.1128	-0.1063
C	-1.11415	0.06025	0.43289	-1.0928	0.0618	0.4487
C	-2.02234	-0.62409	-0.39152	-1.8899	-0.7232	-0.3804
C	-2.87573	-1.59829	0.13215	-2.7337	-1.6802	0.1578
C	-2.83774	-1.90100	1.49079	-2.7899	-1.8689	1.5307
C	-1.94978	-1.22892	2.32670	-2.0004	-1.0916	2.3638
C	-1.09694	-0.25473	1.80207	-1.1588	-0.1313	1.8258
C	1.93595	-1.96876	0.20088	1.8761	-2.1118	0.1222
F	1.96388	-0.95751	1.11652	1.9225	-1.1706	1.0559
F	0.76806	-2.64471	0.39260	0.7307	-2.7627	0.2068
F	2.93463	-2.82932	0.56234	2.8783	-2.9586	0.3079
H	2.19588	1.61109	-2.50733	2.2321	1.6133	-2.4318
H	2.06869	3.89663	-1.59540	2.0578	3.9262	-1.5586
H	0.49352	4.41525	0.25041	0.4413	4.4312	0.2540
H	-0.96863	2.65721	1.16544	-1.0049	2.6447	1.1428
H	-2.07647	-0.39598	-1.45466	-1.8511	-0.5811	-1.4532
H	-3.57117	-2.11841	-0.52174	-3.3497	-2.2828	-0.4984
H	-3.50094	-2.65981	1.89809	-3.4480	-2.6205	1.9494
H	-1.91799	-1.46404	3.38749	-2.0350	-1.2358	3.4368
H	-0.40380	0.25132	2.47184	-0.5298	0.4646	2.4771

Table A.3.: Comparison of the initial (X, Y, Z) and with ωB97X-D3/def2-TZVPD CPCM(DMSO) optimized geometry (X_{opt}, Y_{opt}, Z_{opt}) in Å of biphenyl triflate radical anion.

Atom	X [Å]	Y [Å]	Z [Å]	X_{opt} [Å]	Y_{opt} [Å]	Z_{opt} [Å]
O	2.21087	-2.34272	-2.40298	2.1638	-2.1593	-2.6032
S	2.26542	-1.23125	-1.46304	2.2084	-1.1290	-1.6246
O	3.39312	-0.31289	-1.53212	3.3291	-0.2599	-1.5195

O	0.85979	-0.40162	-1.63562	0.8639	-0.3647	-1.7404
C	0.70905	0.85784	-1.10609	0.6392	0.9281	-1.1458
C	1.45883	1.92285	-1.61556	1.3043	1.9869	-1.7089
C	1.28967	3.20631	-1.10048	1.2347	3.2519	-1.1234
C	0.35576	3.43229	-0.09440	0.5167	3.3689	0.0840
C	-0.42009	2.37575	0.38810	-0.1580	2.3056	0.6257
C	-0.26991	1.07076	-0.11563	-0.2162	1.0098	0.0017
C	-1.12957	-0.01125	0.39528	-1.0877	-0.0191	0.4756
C	-1.96698	-0.73973	-0.46544	-1.5752	-1.0814	-0.3456
C	-2.77719	-1.76884	0.02040	-2.4496	-2.0324	0.1350
C	-2.76632	-2.08345	1.37683	-2.9011	-2.0112	1.4586
C	-1.94872	-1.36857	2.24824	-2.4448	-0.9801	2.2851
C	-1.13904	-0.33948	1.76143	-1.5762	-0.0160	1.8186
C	2.04309	-1.85148	0.24908	2.1050	-1.9892	0.0115
F	1.97951	-0.85040	1.17407	1.9972	-1.1138	0.9979
F	0.91223	-2.59816	0.39497	1.0788	-2.8213	0.0403
F	3.07910	-2.65461	0.63665	3.2287	-2.6822	0.1710
H	2.17742	1.76677	-2.41700	1.9082	1.8168	-2.5925
H	1.88253	4.03056	-1.48973	1.7432	4.0972	-1.5676
H	0.21821	4.43388	0.30597	0.4801	4.3257	0.5952
H	-1.16521	2.58163	1.15521	-0.7215	2.4652	1.5369
H	-1.99930	-0.50375	-1.52774	-1.2790	-1.1342	-1.3843
H	-3.41794	-2.32251	-0.66124	-2.7989	-2.8079	-0.5401
H	-3.39588	-2.88494	1.75471	-3.5870	-2.7635	1.8285
H	-1.93818	-1.61285	3.30739	-2.7704	-0.9362	3.3200
H	-0.50028	0.19984	2.45874	-1.2357	0.7455	2.5103

Table A.4.: Comparison of the initial (X, Y, Z) and with ωB97X-D3/def2-TZVPD optimized geometry (in vacuum) (X_{opt}, Y_{opt}, Z_{opt}) in Å of biphenyl triflate radical anion.

Atom	X [Å]	Y [Å]	Z [Å]	X_{opt} [Å]	Y_{opt} [Å]	Z_{opt} [Å]
O	2.21087	-2.34272	-2.40298	1.9179	-2.3323	-2.5205
S	2.26542	-1.23125	-1.46304	2.1258	-1.1873	-1.7052
O	3.39312	-0.31289	-1.53212	3.2887	-0.3828	-1.8535
O	0.85979	-0.40162	-1.63562	0.8144	-0.3688	-1.7673
C	0.70905	0.85784	-1.10609	0.6392	0.9164	-1.1373
C	1.45883	1.92285	-1.61556	1.3517	1.9655	-1.6539
C	1.28967	3.20631	-1.10048	1.3001	3.2199	-1.0440
C	0.35576	3.43229	-0.09440	0.5340	3.3340	0.1310
C	-0.42009	2.37575	0.38810	-0.1820	2.2784	0.6288
C	-0.26991	1.07076	-0.11563	-0.2363	0.9896	-0.0062

C	-1.12957	-0.01125	0.39528	-1.1112	-0.0404	0.4577
C	-1.96698	-0.73973	-0.46544	-1.6001	-1.1008	-0.3639
C	-2.77719	-1.76884	0.02040	-2.4781	-2.0469	0.1133
C	-2.76632	-2.08345	1.37683	-2.9384	-2.0240	1.4335
C	-1.94872	-1.36857	2.24824	-2.4785	-0.9970	2.2604
C	-1.13904	-0.33948	1.76143	-1.6034	-0.0393	1.7984
C	2.04309	-1.85148	0.24908	2.1948	-1.8136	0.0365
F	1.97951	-0.85040	1.17407	2.2928	-0.8205	0.9039
F	0.91223	-2.59816	0.39497	1.1419	-2.5550	0.3234
F	3.07910	-2.65461	0.63665	3.2915	-2.5749	0.1395
H	2.17742	1.76677	-2.41700	1.9828	1.7929	-2.5167
H	1.88253	4.03056	-1.48973	1.8527	4.0570	-1.4492
H	0.21821	4.43388	0.30597	0.4915	4.2852	0.6530
H	-1.16521	2.58163	1.15521	-0.7873	2.4378	1.5122
H	-1.99930	-0.50375	-1.52774	-1.2972	-1.1564	-1.3998
H	-3.41794	-2.32251	-0.66124	-2.8239	-2.8225	-0.5638
H	-3.39588	-2.88494	1.75471	-3.6284	-2.7744	1.8006
H	-1.93818	-1.61285	3.30739	-2.8040	-0.9534	3.2960
H	-0.50028	0.19984	2.45874	-1.2507	0.7134	2.4932

A.1.2. Benchmark DFT functionals

A DFT benchmark was carried out using the different DFT functionals: PBE0, B3LYP, BHandHLYP, CAM-B3LYP and ωB97X-D3. Fig. A.1 shows the absorption spectra calculated at a TD-DFT/def2-TZVPD level of theory using the different DFT functionals together with the experimental spectrum in gray. The experimental spectrum exhibits a broad absorption band at 3.31 - 3.85 eV with an absorption maximum located at 3.54 eV (350 nm). All tested functionals predict qualitatively similar absorption behavior with four bright absorption features at ca. 2.2, 3.0, 3.7 and 4.7 eV.

To compare the theoretical spectra consistently, the first bright excitation (at around 2.2 eV) was referenced to the experimental absorption maximum. Otherwise, aligning the higher-energy absorption manifold to the experiment would result in an additional intense low-energy absorption feature predicted by TD-DFT that is not observed experimentally is obtained.

The dominant low-energy absorptions were predicted to be at 2.18 eV with PBE0, 2.33 eV with B3LYP, 2.32 eV with BHandHLYP, 2.26 eV with CAM-B3LYP, and 2.31 eV with ωB97X-D3, corresponding to shifts of +1.36, +1.21, +1.22, +1.28, and +1.23 eV relative to the experiment, respectively.

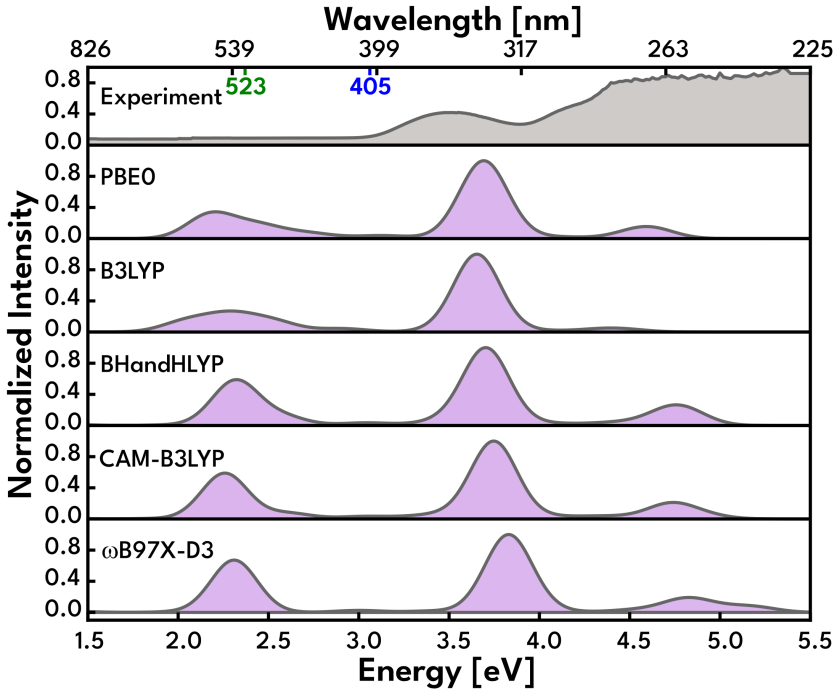

Figure A.1.: Benchmark of different DFT functionals. A FWHM of 0.3 eV was used for the theoretical spectrum. The experimental spectrum is shown on the top.

The ωB97X-D3 functional was for the TD-DFT calculations in the main manuscript for TD-DFT as the investigated system is a diffuse, resonance state with excited states exhibiting signific-

ant CT character. Consequently, long-range effects are expected to play a crucial role in the excited state of biphenyl triflate radical anion. Thus, despite having a larger shift to the experiment than B3LYP and BHandHLYP, ωB97X-D3 was considered to return the most physically meaningful description with TD-DFT of the system.

A.1.3. Vibrational Modes

Tab. A.5 shows the frequency in cm^{-1} and molar extinction coefficient in M^{-1} cm^{-1} of biphenyl triflate radical anion with CPCM(DMSO).

Table A.5.: Calculated vibrational frequencies and molar extinction coefficient (ε) of biphenyl triflate radical anion with DFT in CPCM(DMSO). Symmetric and asymmetric stretching modes are denoted by s and a, respectively, while coupled vibrational (C–H) motions in the biphenyl fragment are abbreviated as CMB.

Frequency [cm^{-1}]	ε [M^{-1} cm^{-1}]	Character of the vibrational mode
15	370	CMB + stretch (as) O_4–S_5–O_6 + stretch (s) C_4–$F_{1,2,3}$
43	151	CMB + stretch (s) O_4–S_5–O_6 + stretch (s) C_4–$F_{1,2,3}$
58	83	CMB + stretch (as) O_4–S_5–O_6 + stretch (as) C_4–$F_{1,2,3}$
66	18	CMB + stretch (as) O_4–S_5–O_6 + stretch (as) C_4–$F_{1,2,3}$
93	10	CMB + stretch (s) O_4–S_5–O_6 + stretch (s) C_4–$F_{1,2,3}$
113	39	CMB + stretch (s) O_4–S_5–O_6 + stretch (as) C_4–$F_{1,2,3}$
120	40	CMB + stretch (s) O_4–S_5–O_6 + stretch (s) C_4–$F_{1,2,3}$
159	77	CMB + stretch (s) O_4–S_5–O_6 + stretch (s) C_4–$F_{1,2,3}$
199	82	CMB + stretch (as) O_4–S_5–O_6 + stretch (s) C_4–$F_{1,2,3}$
207	126	CMB + stretch (as) O_4–S_5–O_6 + stretch (as) C_4–$F_{1,2,3}$
260	188	CMB + stretch (s) O_4–S_5–O_6 + stretch (as) C_4–$F_{1,2,3}$
276	9	CMB + stretch (as) O_4–S_5–O_6 + stretch (as) C_4–$F_{1,2,3}$
300	69	CMB + stretch (s) O_4–S_5–O_6 + stretch (s) C_4–$F_{1,2,3}$
309	34	CMB + stretch (as) O_4–S_5–O_6 + stretch (s) C_4–$F_{1,2,3}$
337	9	CMB + stretch (as) O_4–S_5–O_6 + stretch (s) C_4–$F_{1,2,3}$
340	20	CMB + stretch (s) O_4–S_5–O_6 + stretch (s) C_4–$F_{1,2,3}$
395	215	CMB + stretch (as) O_4–S_5–O_6 + stretch (s) C_4–$F_{1,2,3}$
428	140	CMB
440	83	CMB
473	42	CMB
482	470	CMB + stretch (as) O_4–S_5–O_6 + stretch (s) C_4–$F_{1,2,3}$
523	187	CMB + stretch (as) O_4–S_5–O_6 + stretch (as) C_4–$F_{1,2,3}$
533	92	CMB + stretch (as) O_4–S_5–O_6 + stretch (as) C_4–$F_{1,2,3}$
560	24	CMB + stretch (s) C_4–$F_{1,2,3}$
575	245	CMB + stretch (s) O_4–S_5–O_6 + stretch (as) C_4–$F_{1,2,3}$
603	71	CMB
612	1446	CMB + stretch (s) O_4–S_5–O_6 + stretch (s) C_4–$F_{1,2,3}$
624	104	CMB
639	15	CMB
668	844	CMB
687	96	CMB
697	659	CMB

720	113	CMB
736	343	CMB
770	132	CMB + stretch (s) O_4–S_5–O_6 + stretch (s) C_4–$F_{1,2,3}$
792	197	CMB
801	338	CMB + stretch (s) O_4–S_5–O_6 + stretch (s) C_4–$F_{1,2,3}$
821	69	CMB
847	235	CMB
894	2117	stretch (s) S_5O_8
926	262	CMB
972	2847	CMB
979	644	CMB
987	19	CMB
994	4	CMB
1019	289	CMB
1040	1113	CMB
1045	23	CMB
1078	651	CMB + stretch (as) C_9O8
1108	71	CMB
1131	470	CMB
1145	599	CMB + stretch (s) O_4–S_5–O_6 + stretch (as) C_4–$F_{1,2,3}$
1155	743	CMB
1170	342	CMB
1197	1826	stretch (as) C_4–$F_{1,2,3}$
1216	448	CMB
1223	1097	stretch (as) $C_4F_2F_3 + CMB$
1258	238	CMB + stretch (s) O_4–S_5–O_6
1266	388	CMB + stretch (as) O_4–S_5–O_6 + stretch (s) C_4–$F_{1,2,3}$
1315	237	CMB
1339	184	CMB
1363	303	CMB
1373	359	CMB
1419	157	CMB + stretch (as) O_4–S_5–O_6
1423	1173	CMB + stretch (as) O_4–S_5–O_6
1482	5	CMB
1486	9	CMB
1527	49	CMB
1537	688	CMB
1557	44	CMB
1611	5475	CMB
1673	1	CMB
3168	67	CMB
3172	44	CMB
3177	51	CMB

3195	17	CMB
3205	14	CMB
3209	37	CMB
3212	63	CMB
3225	17	CMB
3234	21	CMB

A.1.4. CASSCF Space Orbital Characterization

Fig. A.2 shows the π^* orbitals of the CASSCF active space shown in Fig. 3.1, zoomed in with an isovalue of 0.01 a.u to identify σ^*(S–O) contributions.

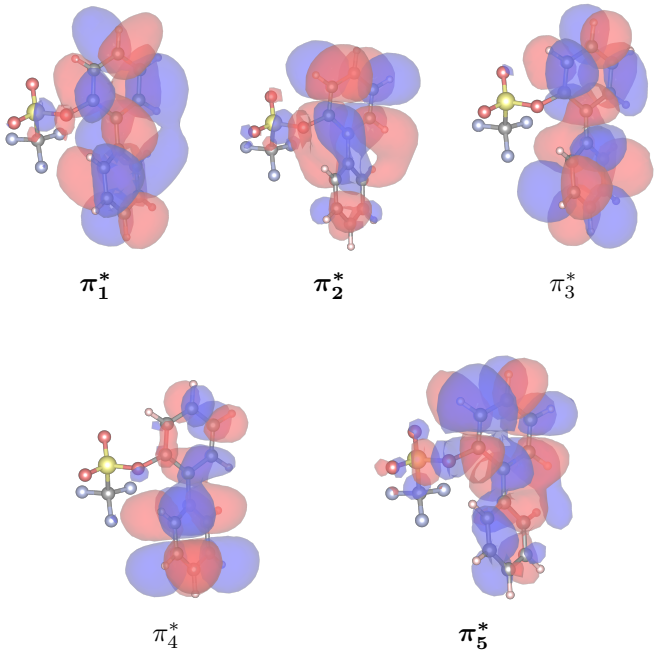

Figure A.2.: Franck-Condon π^* active space orbitals of the biphenyl triflate radical anion with an isosurface cutoff value of 0.01 a.u., calculated with SA_{10}(9, 9) CASSCF/def2-TZVPD with ASS1ST protocol. Orbitals with σ^*(S–O) contributions are labeled bold. Molecules are colored by element (C: gray, F: light red, O: dark red and S: yellow).

A.1.5. State Correlation Diagram

Tab. A.6 lists the coordinates of the DFT optimized dissociated structures used for the state correlation diagram in Fig. 4.12.

Table A.6.: Geometries of with ωB97X-D3/def2-TZVPD CPCM(DMSO) optimized dissociated structures (left: r(S–O) = 10.35 Å and right: r(C–O) = 10.24 Å.

Atom	X [Å]	Y [Å]	Z [Å]	X_{opt} [Å]	Y_{opt} [Å]	Z_{opt} [Å]
O	7.59042	-6.43502	-0.03719	4.10409	-7.29421	-3.74740
S	8.23070	-5.10062	-0.17807	4.75666	-6.36646	-2.85052
O	7.23502	-3.99829	-0.23037	5.86990	-6.91588	-2.10910
O	-0.73721	0.06763	-0.10013	4.97896	-5.04565	-3.39462
C	-0.80624	1.30953	-0.06522	-0.29226	3.20503	-0.39282
C	0.35829	2.11453	-0.37569	0.10186	4.37303	-0.98295
C	0.33012	3.47177	-0.27073	-0.64253	5.51130	-0.66771
C	-0.85347	4.11643	0.13493	-1.71804	5.40977	0.20539
C	-2.00626	3.38524	0.41990	-2.06435	4.19149	0.77376
C	-2.03479	2.00946	0.31991	-1.33810	3.02848	0.48599
C	-3.26918	1.25497	0.60748	-1.66349	1.70596	1.07214
C	-3.70196	0.22742	-0.23348	-1.36036	0.53925	0.36997
C	-4.88676	-0.44235	0.02671	-1.65245	-0.70589	0.90400
C	-5.65133	-0.10730	1.13656	-2.25352	-0.80583	2.15165
C	-5.22764	0.90839	1.98215	-2.55634	0.34861	2.86021
C	-4.04844	1.58734	1.71705	-2.26270	1.59451	2.32600
C	8.70843	-5.17731	-2.00542	3.48386	-6.07897	-1.54549
F	9.24978	-4.01840	-2.41270	3.92977	-5.22014	-0.62377
F	9.62014	-6.13968	-2.21986	2.36379	-5.57303	-2.06954
F	7.65865	-5.43225	-2.79629	3.16769	-7.21899	-0.92438
H	1.25276	1.58201	-0.67606	0.94737	4.42473	-1.65906
H	1.21102	4.05998	-0.49687	-0.37935	6.46687	-1.10637
H	-0.87620	5.19622	0.21468	-2.30125	6.29100	0.44411
H	-2.90732	3.91674	0.70259	-2.91861	4.13521	1.43953
H	-3.11501	-0.03518	-1.10389	-0.89949	0.61289	-0.60903
H	-5.21494	-1.22900	-0.64235	-1.41351	-1.60047	0.34098
H	-6.57439	-0.63678	1.34092	-2.48210	-1.77863	2.57053
H	-5.81570	1.17257	2.85309	-3.01783	0.28042	3.83833
H	-3.71851	2.37190	2.38836	-2.48767	2.48559	2.90019

A.2. Non-Hermitian Electronic Structure Calculations

Python code Lst. A.2 was used to determine optimal smooth-Voronoi pCAP cutoff radius in the PyOpenCAP package.

Listing A.2: Determination of the optimal smooth-Voronoi pCAP cutoff radius r_{cut} in the PyOpenCAP package using an input RASCI Hamiltonian. Python code was formatted using GPT-5.3 by OpenAI.

```python
#!/usr/bin/env python3
"""
Determination of the optimal Voronoi CAP cutoff radius (r_cut)

The optimal r_cut is selected based on the stability of the CAP
eigenvalue trajectory. As a quantitative measure, the logarithmic
velocity |eta dE/deta| evaluated at eta_opt is minimized.
"""

import os
import re
import numpy as np
import pandas as pd
import matplotlib.pyplot as plt
import pyopencap
from pyopencap.analysis import CAPHamiltonian

# ==============================
# Input parameters
# ==============================

WORKDIR = "/path/to/working/directory"
RASSI_FILE = os.path.join(WORKDIR, "filename.rassi.h5")
LOG_FILE = os.path.join(WORKDIR, "filename.log")

NSTATES = 30
R_CUT_VALUES = np.arange(1.0, 4.1, 0.1)
ETA_GRID = np.linspace(0.0, 5.0e-2, 101)


# ==============================
# Extract RASSI energies
# ==============================

def parse_rassi_energies(log_file, nstates):
    energies = []

    with open(log_file, "r") as f:
        for line in f:
            match = re.search(
                r"RASSI State\s+(\d+)\s+Total energy:\s+([-+]?[\d\s
```

```
    ]+\.[ \dE+-]+)",
                line
            )
            if match:
                idx = int(match.group(1))
                energy = float(match.group(2))

                if idx <= nstates:
                    while len(energies) < idx:
                        energies.append(0.0)
                    energies[idx - 1] = energy

    return np.array(energies)


# ==============================
# r_cut scan
# ==============================

def compute_optimal_rcut():

    rassi_energies = parse_rassi_energies(LOG_FILE, NSTATES)
    H0 = np.diag(rassi_energies)

    results = []

    for r_cut in R_CUT_VALUES:

        cap_dict = {
            "cap_type": "voronoi",
            "r_cut": f"{r_cut:.1f}",
            "Radial_precision": "15",
            "angular_points": "150"
        }

        system = pyopencap.System({
            "molecule": "molcas_rassi",
            "basis_file": RASSI_FILE
        })

        cap = pyopencap.CAP(system, cap_dict, NSTATES)

        cap.read_data({
            "package": "openmolcas",
            "rassi_h5": RASSI_FILE,
            "method": "ms-caspt2"
        })

        cap.compute_projected_cap()
```

```
        W = cap.get_projected_cap()

        capH = CAPHamiltonian(H0=H0, W=W)
        capH.run_trajectory(ETA_GRID)

        traj = capH.track_state(0, tracking="overlap")

        _, eta_opt = traj.find_eta_opt(
            corrected=True,
            start_idx=10,
            end_idx=-1,
            ref_energy=np.min(H0),
            units="eV"
        )

        idx = np.argmin(np.abs(ETA_GRID - eta_opt))

        idx_left = max(0, idx - 1)
        idx_right = min(len(ETA_GRID) - 1, idx + 1)

        eta_left = ETA_GRID[idx_left]
        eta_right = ETA_GRID[idx_right]

        e_left = traj.get_energy(eta_left, corrected=True)
        e_right = traj.get_energy(eta_right, corrected=True)

        dE_deta = (e_right - e_left) / (eta_right - eta_left)

        log_velocity = abs(eta_opt * dE_deta)

        results.append({
            "r_cut": r_cut,
            "eta_opt": eta_opt,
            "log_velocity": log_velocity
        })

    return pd.DataFrame(results)


# ==============================
# Run analysis
# ==============================

df = compute_optimal_rcut()

optimal_idx = df["log_velocity"].idxmin()
r_cut_opt = df.loc[optimal_idx, "r_cut"]
eta_opt = df.loc[optimal_idx, "eta_opt"]
```

```
139
140 # ==============================
141 # Plot results
142 # ==============================
143
144 plt.figure()
145 plt.plot(df["r_cut"], df["log_velocity"], marker="o")
146 plt.axvline(r_cut_opt, linestyle="--",
147             label=f"r_cut = {r_cut_opt:.1f} Å")
148
149 plt.xlabel(r"$r_{\mathrm{cut}}$ (a_0)")
150 plt.ylabel(r"$|\eta \, dE/d\eta|$")
151 plt.legend()
152 plt.grid()
153
154 plt.savefig(os.path.join(WORKDIR, "rcut_optimization.png"), dpi=300)
155
156
157 # ==============================
158 # Save results
159 # ==============================
160
161 df.to_csv(os.path.join(WORKDIR, "rcut_scan.csv"), index=False)
```

Fig. A.3 shows the dependence of the smooth Voronoi cutoff radius r_{cut} of the pCAP η trajectories. The optimization criterion $|\eta \frac{dE_{CAP}(\eta)}{d\eta}|$ (see also Eq. (32)) shows a minimum at a r_{cut} value of 1.9 a_0, indicating the optimal η value. For larger values of r_{cut}, the optimization criterion decreases again without forming another minimum as the effect of the CAP becomes continuously smaller, leading to a reduced sensitivity of the complex resonance energy to variations of η.

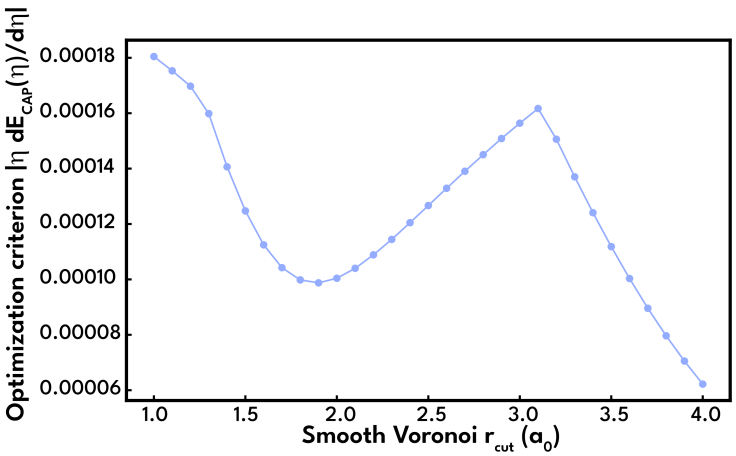

Figure A.3.: Smooth Voronoi cutoff radius optimization.

Python code Lst. A.3 was used to determine optimal η values for each state for pCAP-RASCI in the PyOpenCAP package.

Listing A.3: pCAP eta trajectory analysis in PyOpenCAP. Python code was formatted using GPT-5.3 by OpenAI.

```
1
2  #!/usr/bin/env python3
3  """
4  pCAP -trajectory analysis for all states
5  """
6
7  import os
8  import re
9  import numpy as np
10 import matplotlib.pyplot as plt
11 import pyopencap
12 from pyopencap.analysis import CAPHamiltonian
13
14 # ==============================
15 # Input parameters
16 # ==============================
17
18 working_dir = "/path/to/working/dir"
19 RASSI_FILE = os.path.join(working_dir, "MOLCAS.rassi.h5")
20 OUTPUT_FILE = os.path.join(working_dir, "MOLCAS.log")
21 nstates = 30  # number of states
22
23 # CAP parameters
24 cap_dict = {
25     "cap_type": "voronoi",
26     "r_cut": "1.9",
27     "Radial_precision": "15",
28     "angular_points": "150"
29 }
30
31 # ==============================
32 # Build system
33 # ==============================
34
35 system = pyopencap.System({"molecule": "molcas_rassi", "basis_file":
       RASSI_FILE})
36
37 # ==============================
38 # Parse RASSI energies
39 # ==============================
40
41 def parse_rassi_energies(log_file, nstates):
42     energies = [np.nan]*nstates
43     with open(log_file, "r") as f:
```

```
        for line in f:
            m = re.search(r"RASSI State\s+(\d+)\s+Total energy:\s+([-+]?[\d\s]+\.[\dE+-]+)", line)
            if m:
                idx = int(m.group(1)) - 1
                if 0 <= idx < nstates:
                    energies[idx] = float(m.group(2))
    return np.array(energies)

rassi_energies = parse_rassi_energies(OUTPUT_FILE, nstates)
H0 = np.diag(rassi_energies)

# ==============================
# Build CAP
# ==============================

cap = pyopencap.CAP(system, cap_dict, nstates)
cap.read_data({"package": "openmolcas", "rassi_h5": RASSI_FILE, "method": "ms-caspt2"})
cap.renormalize()
cap.compute_projected_cap()
W = cap.get_projected_cap()

# ==============================
# Construct CAP Hamiltonian
# Run eta trajectories
# ==============================

CAPH = CAPHamiltonian(H0=H0, W=W)
eta_list = np.linspace(0, 0.05, 101)  # small eta grid for stability
CAPH.run_trajectory(eta_list)
ref_energy = np.min(H0)

# ==============================
# Analyze all states
# ==============================

results = []
for i in range(nstates):
    traj = CAPH.track_state(i, tracking="overlap")
    uc_E_ev, uc_eta = traj.find_eta_opt(start_idx=10, ref_energy=ref_energy, units="eV")
    corr_E_ev, corr_eta = traj.find_eta_opt(corrected=True, start_idx=10, end_idx=-1, ref_energy=ref_energy, units="eV")
    results.append({
        "state": i+1,
        "traj": traj,
        "uc_eta": uc_eta,
        "uc_E": uc_E_ev,
```

```
89          "corr_eta": corr_eta,
90          "corr_E": corr_E_ev
91      })
92
93  # ==============================
94  # Plot eta trajectories
95  # ==============================
96
97  fig, ax = plt.subplots(figsize=(10,8))
98  for r in results:
99      traj = r["traj"]
100     re_corr = np.real(traj.energies_ev(ref_energy, corrected=True))
101     im_corr = np.imag(traj.energies_ev(ref_energy, corrected=True))
102     ax.plot(re_corr, im_corr, "-o", alpha=0.5, label="State 1" if r["
        state"]==1 else "")
103 ax.set_xlabel("Re(E) [eV]")
104 ax.set_ylabel("Im(E) [eV]")
105 ax.set_title("CAP  Trajectories (all states)")
106 ax.grid(True)
107 plt.tight_layout()
108 plt.savefig(os.path.join(working_dir, "CAP_eta_trajectories.png"),
        dpi=300)
109 plt.show()
```

Tab. A.7 shows the uncorrected and first-order corrected η value and resonance position (E_{UC}/E_C^1) and resonance width (Γ_{UC}/Γ_C^1), calculated with pCAP-RASCI (see Eq. (35)). The quantities reported in Tab. A.7 were used to identify electronic resonance states based on magnitude of η. States with η < 0.1 were considered to have a sufficiently stable pCAP behavior and they were therefore identified as resonances. The lifetimes of the resonance states were extracted from the corrected resonance width, Γ_C^1 through Eq. (38).

State	η_{UC}	E_{UC} (a.u.)	Γ_{UC} (a.u.)	$\eta_C^{(1)}$	$E_C^{(1)}$ (a.u.)	Γ_C^1
1	0.010	-1418.3665	-0.087375	0.056	-1418.3664	-0.000146
2	0.010	-1418.3102	-0.195519	0.999	-1418.2909	-0.000892
3	0.010	-1418.2903	-0.384445	0.999	-1418.2879	0.000194
4	0.010	-1418.3055	-0.202163	0.999	-1418.2774	-0.000289
5	0.010	-1418.2813	-0.445710	0.999	-1418.2808	0.000093
6	0.010	-1418.3015	-0.255244	0.206	-1418.2945	0.000830
7	0.010	-1418.2989	-0.196567	0.999	-1418.2821	0.000237
8	0.010	-1418.2930	-0.206967	0.999	-1418.2796	-0.000864
9	0.010	-1418.2903	-0.384445	0.999	-1418.2879	0.000194
10	0.010	-1418.2910	-0.259025	0.999	-1418.2900	0.000307
11	0.010	-1418.2738	-0.213885	0.999	-1418.2713	0.001395
12	0.010	-1418.2758	-0.203176	0.999	-1418.2730	-0.000454
13	0.010	-1418.2549	-0.228211	0.446	-1418.2620	0.000541
14	0.010	-1418.2616	-0.220240	0.061	-1418.2586	0.005344
15	0.010	-1418.2551	-0.086658	0.024	-1418.2552	-0.000409
16	0.010	-1418.2657	-0.229009	0.999	-1418.2659	-0.000021
17	0.010	-1418.2597	-0.252217	0.999	-1418.2607	-0.000334
18	0.010	-1418.2646	-0.740135	0.999	-1418.2646	0.000042
19	0.010	-1418.2464	-0.227773	0.999	-1418.2592	0.000229
20	0.010	-1418.2297	-0.087521	0.029	-1418.2302	-0.001302
21	0.010	-1418.2357	-0.195261	0.999	-1418.2659	-0.000723
22	0.010	-1418.2339	-0.212589	0.999	-1418.2633	0.000123
23	0.010	-1418.2193	-0.087472	0.198	-1418.2199	0.000986
24	0.010	-1418.2193	-0.087472	0.198	-1418.2199	0.000986
25	0.010	-1418.2011	-0.231850	0.151	-1418.2010	0.000029
26	0.010	-1418.1990	-0.095800	0.999	-1418.2011	0.000214
27	0.010	-1418.2020	-0.211215	0.999	-1418.2020	0.000029
28	0.010	-1418.1949	-0.284604	0.999	-1418.1950	-0.000017
29	0.010	-1418.1904	-0.392454	0.951	-1418.1904	0.000001
30	0.010	-1418.1939	-0.311911	0.999	-1418.1939	0.000028

Table A.7.: pCAP-RASCI states with uncorrected (labeled as UC) and corrected (labeled as C) η values with corresponding resonance positions E and widths Γ.

Bibliography

[1] Blanc, A.; Bochet, C. G. Wavelength-Controlled Orthogonal Photolysis of Protecting Groups. The Journal of Organic Chemistry **2002**, 67, 5567–5577.

[2] Hoffmann, N. Photochemical Reactions as Key Steps in Organic Synthesis. Chemical Reviews **2008**, 108, 1052–1103.

[3] Protti, S.; Ravelli, D.; Fagnoni, M. Wavelength dependence and wavelength selectivity in photochemical reactions. Photochem. Photobiol. Sci. **2019**, 18, 2094–2101.

[4] Bogdanova, A.; Popik, V. V. Wavelength-Dependent Photochemistry of Diazo Meldrum's Acid and Its Spirocyclic Isomer, Diazirino Meldrum's Acid: Wolff Rearrangement versus Isomerization. Journal of the American Chemical Society **2003**, 125, 1456–1457.

[5] Maafi, M. Excitation Wavelength-Dependent Photochemistry. Photochem **2024**, 4, 233–270.

[6] Howells, R. D.; Mc Cown, J. D. Trifluoromethanesulfonic acid and derivatives. Chemical Reviews **1977**, 77, 69–92.

[7] Frantz, D. E.; Weaver, D. G.; Carey, J. P.; Kress, M. H.; Dolling, U. H. Practical Synthesis of Aryl Triflates under Aqueous Conditions. Organic Letters **2002**, 4, 4717–4718.

[8] Portolés, F. G.; Bonifazi, D. Private communication. **2025**.

[9] Jagau, T.-C. Theory of electronic resonances: fundamental aspects and recent advances. Chem. Commun. **2022**, 58, 5205–5224.

[10] Herbert, J. M. Reviews in Computational Chemistry Volume 28; John Wiley Sons, Ltd, **2015**; Chapter 8, pp 391–517.

[11] Schrödinger, E. An Undulatory Theory of the Mechanics of Atoms and Molecules. Physical Review **1926**, 28, 1049–1070.

[12] Born, M.; Oppenheimer, R. Zur Quantentheorie der Molekeln. Annalen der Physik **1927**, 389, 457–484.

[13] Koch, W.; Holthausen, M. C. A Chemist's Guide to Density Functional Theory; Wiley-VCH Verlag GmbH, **2001**.

[14] Deskevich, M. P.; Nesbitt, D. J.; Werner, H.-J. Dynamically weighted multiconfiguration self-consistent field: Multistate calculations for F+H2O HF+OH reaction paths. The Journal of Chemical Physics **2004**, 120, 7281–7289.

[15] Jensen, F. Introduction to Computational Chemistry 3rd. ed., 3rd ed.; Wiley, **2017**.

[16] Malmqvist, P.; Rendell, A.; Roos, B. The restricted active space self-consistent-field method, implemented with a split graph unitary group approach. Journal of Physical Chemistry **1990**, 94, 5477–5482.

[17] Angeli, C.; Cimiraglia, R.; Evangelisti, S.; Leininger, T.; Malrieu, J.-P. Introduction of n-electron valence states for multireference perturbation theory. The Journal of Chemical Physics **2001**, 114, 10252–10264.

[18] Dai, Y.; Wei, W.; Ma, Y.; Niu, C. In Calculations and Simulations of Low-Dimensional Materials: Tailoring Properties for Applications; Dai, Y., Wei, W., Ma, Y., Niu, C., Eds.; John Wiley & Sons, Ltd, **2022**; Chapter 1, pp 1–15.

[19] Hohenberg, P.; Kohn, W. Inhomogeneous Electron Gas. Physical Review **1964**, 136, B864–B871.

[20] Kohn, W.; Sham, L. J. Self-Consistent Equations Including Exchange and Correlation Effects. Phys. Rev. **1965**, 140, A1133–A1138.

[21] Lee, C.; Yang, W.; Parr, R. G. Development of the Colle-Salvetti correlation-energy formula into a functional of the electron density. Phys. Rev. B **1988**, 37, 785–789.

[22] Becke, A. D. Density functional thermochemistry. III. The role of exact exchange. The Journal of Chemical Physics **1993**, 98, 5648–5652.

[23] Grimme, S.; Antony, J.; Ehrlich, S.; Krieg, H. A consistent and accurate ab initio parametrization of density functional dispersion correction (DFT-D) for the 94 elements H-Pu. The Journal of Chemical Physics **2010**, 132, 154104.

[24] von Barth, U.; Hedin, L. A local exchange-correlation potential for the spin polarized case. i. Journal of Physics C: Solid State Physics **1972**, 5, 1629.

[25] A Chemist's Guide to Density Functional Theory; John Wiley Sons, Ltd, **2001**; Chapter 1, pp 3–18.

[26] Runge, E.; Gross, E. K. U. Density-Functional Theory for Time-Dependent Systems. Physical Review Letters **1984**, 52, 997–1000.

[27] van Leeuwen, R. Beyond the Runge-Gross Theorem. Lecture Notes in Physics **2006**, 706.

[28] Huix-Rotllant, M.; Ferré, N.; Barbatti, M. Quantum Chemistry and Dynamics of Excited States; **2020**; pp 13–46.

[29] Marques, M.; Ullrich, C.; Nogueira, F.; Rubio, A.; Burke, K.; Gross, E. Time-Dependent Density Functional Theory; Lecture Notes in Physics; Springer Berlin Heidelberg, **2006**.

[30] Tamm, I. Selected Papers; Springer, **1991**; pp 157–174.

[31] Dancoff, S. M. Non-Adiabatic Meson Theory of Nuclear Forces. Physical Review **1950**, 78, 382–385.

[32] Siegert, A. J. F. On the Derivation of the Dispersion Formula for Nuclear Reactions. Phys. Rev. **1939**, 56, 750–752.

[33] Riss, U.; Meyer, H.-D. Calculation of resonance energies and widths using the complex absorbing potential method. Journal of Physics B: Atomic, Molecular and Optical Physics **1993**, 26, 4503.

[34] Sommerfeld, T.; Ehara, M. Complex Absorbing Potentials with Voronoi Isosurfaces Wrapping Perfectly around Molecules. Journal of Chemical Theory and Computation **2015**, 11, 4627–4633.

[35] Ehara, M.; Sommerfeld, T. CAP/SAC-CI method for calculating resonance states of metastable anions. Chemical Physics Letters **2012**, 537, 107–112.

[36] Jagau, T.-C.; Zuev, D.; Bravaya, K. B.; Epifanovsky, E.; Krylov, A. I. A Fresh Look at Resonances and Complex Absorbing Potentials: Density Matrix-Based Approach. The Journal of Physical Chemistry Letters **2014**, 5, 310–315.

[37] Thodika, M.; Matsika, S. Projected Complex Absorbing Potential Multireference Configuration Interaction Approach for Shape and Feshbach Resonances. Journal of Chemical Theory and Computation **2022**, 18, 3377–3390.

[38] Neese, F. Software Update: The ORCA Program System—Version 6.0. WIREs Computational Molecular Science **2025**, 15, e70019.

[39] Landrum, G. RDKit: Open-source cheminformatics. Journal of Cheminformatics **2013**, 5, 1–10.

[40] Halgren, T. A. Merck molecular force field. I. Basis, form, scope, parameterization, and performance of MMFF94. Journal of Computational Chemistry **1996**, 17, 490–519.

[41] Halgren, T. A. Merck molecular force field. II. MMFF94 van der Waals and electrostatic parameters for intermolecular interactions. Journal of Computational Chemistry **1996**, 17, 520–552.

[42] Halgren, T. A. Merck molecular force field. III. Molecular geometries and vibrational frequencies for MMFF94. Journal of Computational Chemistry **1996**, 17, 553–586.

[43] Halgren, T. A.; Nachbar, R. B. Merck molecular force field. IV. conformational energies and geometries for MMFF94. Journal of Computational Chemistry **1996**, 17, 587–615.

[44] Halgren, T. A. Merck molecular force field. V. Extension of MMFF94 using experimental data, additional computational data, and empirical rules. Journal of Computational Chemistry **1996**, 17, 616–641.

[45] Chai, J.; Head-Gordon, M. Long-range corrected hybrid density functionals with damped atom–atom dispersion corrections. Physical Chemistry Chemical Physics **2008**, 10, 6615–6620.

[46] Chai, J.; Head-Gordon, M. Systematic Optimization of Long-Range Corrected Hybrid Density Functionals. The Journal of Chemical Physics **2008**, 128.

[47] Mardirossian, N.; Head-Gordon, M. ωB97X-D: A hybrid meta-GGA density functional that is broadly accurate for thermochemistry, kinetics, and noncovalent interactions. The Journal of Chemical Physics **2016**, 144, 214110.

[48] Rappoport, D.; Furche, F. Property-optimized Gaussian basis sets for molecular response calculations. J. Chem. Phys. **2010**, 133, 134105.

[49] Weigend, F.; Ahlrichs, R. Balanced basis sets of split valence, triple zeta valence and quadruple zeta valence quality for H to Rn: Design and assessment of accuracy. Phys. Chem. Chem. Phys. **2005**, 7, 3297.

[50] Liang, J.; Feng, X.; Hait, D.; Head-Gordon, M. Revisiting the Performance of Time-Dependent Density Functional Theory for Electronic Excitations: Assessment of 43 Popular and Recently Developed Functionals from Rungs One to Four. Journal of Chemical Theory and Computation **2022**, 18, 3460–3473.

[51] Neese, F.; Wennmohs, F.; Hansen, A.; Becker, U. Efficient, approximate and parallel Hartree–Fock and hybrid DFT calculations. A 'chain-of-spheres' algorithm for the Hartree–Fock exchange. Chemical Physics **2009**, 356, 98–109.

[52] Mennucci, B. Polarizable continuum model. WIREs Computational Molecular Science **2012**, 2, 386–404.

[53] Lipparini, F.; Mennucci, B. Perspective: Polarizable continuum models for quantum-mechanical descriptions. The Journal of Chemical Physics **2016**, 144, 160901–54109.

[54] Hirshfeld, F. L. Bonded-atom fragments for describing molecular charge densities. Theoretica chimica acta **1977**,

[55] Plasser, F. TheoDORE: A toolbox for a detailed and automated analysis of electronic excited state computations. The Journal of Chemical Physics **2020**, 152, 084108.

[56] Frisch, M. J. et al. Gaussian 16 Revision C.01. **2016**; Gaussian Inc. Wallingford CT.

[57] Ugandi, M.; Roemelt, M. A configuration-based heatbath-CI for spin-adapted multireference electronic structure calculations with large active spaces. Journal of Computational Chemistry **2023**, 44, 2374–2390.

[58] Ugandi, M.; Roemelt, M. Analytical SA-HCISCF Nuclear Gradients from Spin-Adapted Heat-Bath Configuration Interaction. Journal of Chemical Theory and Computation **2025**, 21, 3930–3944.

[59] Li Manni, G. et al. The OpenMolcas Web: A Community-Driven Approach to Advancing Computational Chemistry. Journal of Chemical Theory and Computation **2023**, 19, 6933–6991.

[60] Khedkar, A.; Roemelt, M. Active Space Selection Based on Natural Orbital Occupation Numbers from n-Electron Valence Perturbation Theory. Journal of Chemical Theory and Computation **2019**, 15, 3522–3536.

[61] Khedkar, A.; Roemelt, M. Extending the ASS1ST Active Space Selection Scheme to Large Molecules and Excited States. Journal of Chemical Theory and Computation **2020**, 16, 4993–5005.

[62] Khedkar, A.; Roemelt, M. An ab initio multireference study of reductive eliminations from organoferrates(iii) in the gas-phase: it is all about the spin state. Phys. Chem. Chem. Phys. **2020**, 22, 17677–17686.

[63] Gayvert, J. R. OpenCAP: An Open-Source Program for Studying Resonances in Molecules. `https://github.com/gayverjr/opencap`, **2023**; Last Accessed: 2026-04-03.

[64] Arulmozhiraja, S.; Fujii, T. Torsional barrier, ionization potential, and electron affinity of biphenyl—A theoretical study. The Journal of Chemical Physics **2001**, 115, 10589–10594.

[65] Infrared and Raman Spectra of Inorganic and Coordination Compounds; John Wiley Sons, Ltd, **2008**; pp 355–413.

[66] Laurent, A. D.; Jacquemin, D. TD-DFT benchmarks: A review. International Journal of Quantum Chemistry **2013**, 113, 2019–2039.

[67] Ptasińska, S.; Gschliesser, D.; Bartl, P.; Janik, I.; Scheier, P.; Denifl, S. Dissociative electron attachment to triflates. The Journal of Chemical Physics **2011**, 135, 214309.